



LAWRENCE
LIVERMORE
NATIONAL
LABORATORY

Electron and Ion Kinetic Effects on Nonlinearly Driven Electron Plasma and Ion Acoustic Waves

R. L. Berger, S. Brunner, T. Chapman, L. Divol, C.
H. Still, E. J. Valeo

April 12, 2011

Physics of Plasmas

Disclaimer

This document was prepared as an account of work sponsored by an agency of the United States government. Neither the United States government nor Lawrence Livermore National Security, LLC, nor any of their employees makes any warranty, expressed or implied, or assumes any legal liability or responsibility for the accuracy, completeness, or usefulness of any information, apparatus, product, or process disclosed, or represents that its use would not infringe privately owned rights. Reference herein to any specific commercial product, process, or service by trade name, trademark, manufacturer, or otherwise does not necessarily constitute or imply its endorsement, recommendation, or favoring by the United States government or Lawrence Livermore National Security, LLC. The views and opinions of authors expressed herein do not necessarily state or reflect those of the United States government or Lawrence Livermore National Security, LLC, and shall not be used for advertising or product endorsement purposes.

Electron and Ion Kinetic Effects on Non-Linearly Driven Electron Plasma and Ion Acoustic Waves

R. L. Berger,^{1,*} S. Brunner,^{2,†} T. Chapman,¹ L. Divol,¹ C. H. Still,¹ and E. J. Valeo³

¹ *Lawrence Livermore National Laboratory, University of California,
P.O. Box 808, Livermore, California 94551*

² *Centre de Recherches en Physique des Plasmas,
Association Euratom-Confédération Suisse,
Ecole Polytechnique Fédérale de Lausanne,
CRPP-PPB, CH-1015 Lausanne, Switzerland*

³ *Princeton Plasma Physics Laboratory,
P.O. Box 451, Princeton, New Jersey 08543-0451*

(Dated: November 15, 2012)

Abstract

Fully non-linear kinetic simulations of electron plasma (EPWs) and ion acoustic waves (IAWs) have been carried out with a new multi-species, parallelized Vlasov code. The numerical implementation of the Vlasov model and the methods used to compute the wave frequency are described in detail. For the first time, the nonlinear frequency of IAWs, combining the contributions from electron and ion kinetic effects and from harmonic generation, has been calculated and compared to Vlasov results. Excellent agreement of theory with simulation results is shown at all amplitudes, harmonic generation being an essential component at large amplitudes. For IAWs, the positive frequency shift from trapped electrons is confirmed and is dominant for the effective electron-to-ion temperature ratio, $Z T_e/T_i \gtrsim 10$ with Z the charge state. Furthermore, numerical results demonstrate unambiguously the dependence [R.L. Dewar, Phys. Fluids **15**, 712 (1972)] of the kinetic shifts on details of the distribution of the trapped particles, which depends in turn on the conditions under which the waves were generated. The trapped particle fractions and energy distributions are derived and, upon inclusion of harmonic effects, shown to agree with the simulation results, completing a consistent picture. Fluid models of the wave evolution are considered but prove unable to capture essential details of the kinetic simulations. Detrapping by collisions and sideloss are also discussed.

*berger5@llnl.gov

†stephan.brunner@epfl.ch

I. INTRODUCTION

The properties of large-amplitude Electron Plasma Waves (EPWs), also referred to as Langmuir waves, and Ion Acoustic Waves (IAWs) and their self-consistent distribution of trapped particles lies at the heart of much current theoretical research for nonlinear IAWs[1–4], on stimulated Brillouin scattering[5–11], nonlinear EPWs[12–19], and stimulated Raman scattering.[20–32] Our particular interest is laser light propagation in hot, high-density plasma where many processes can create such waves.[33–36] However, similar wave-particle interactions are important in vastly different plasma conditions.[37–39] In all cases, a large-amplitude wave is created which traps particles that support an undamped BGK-like oscillation [40], in the absence of strong inhomogeneity or binary collisions, until various instabilities develop over a longer time scale and destroy this highly coherent state. The seminal work of O’Neil [41] showed in the case of EPW’s, that a large amplitude wave would evolve to a quasi BGK-like state within a few trapping oscillations of the electrons. Subsequently, Morales and O’Neil [42] and Dewar [43] showed that, as a result of the modification of the distribution by resonant electrons, the frequency of the non-linear BGK-like mode is shifted relative to the linear frequency for Maxwell-Boltzmann distributions by an amount proportional to $\sqrt{\phi}$, where ϕ is the amplitude of the electrostatic potential.

Despite the fundamental nature of this research and its long history, a detailed comparison of the nonlinear state produced in kinetic simulations with theoretical models has only begun recently and primarily for EPWs. The frequency of the nonlinear wave is of particular interest because it enters as a parameter in theoretical models, *e.g.* [24, 30]. In all previous work, the small-amplitude kinetic shift is predicted to be proportional to $\sqrt{\phi}$ but with a coefficient that differs according to conditions of wave generation. Dewar indeed showed that such a coefficient was dependent on the physical process by which the wave was produced.[43] If the wave is initialized *suddenly* with a large amplitude, it evolves to a so-called *sudden* distribution of resonant particles. On the other hand, if the wave is driven slowly with respect to the bounce frequency time scale by an external force up to a finite amplitude, it evolves to a so-called *adiabatic* distribution of resonant particles.[12, 13, 43] The bounce frequency is given by $\omega_{b,j} = k\sqrt{e|Z_j|\phi/m_j}$, where the species index $j = e, i$ for electrons and ions respectively, Z_j is the ionization state (in particular $Z_e = -1$), m_j the mass, and k the wavenumber. The sudden distribution produces a shift that is larger than the adiabatic

distribution by the ratio, $\alpha_s/\alpha_{ad} = 0.823/0.544 = 1.51$. In the sudden case, the Dewar results are identical to those obtained by Morales and O’Neil.[42]

Significantly less work has been published on the generation of large amplitude IAWs and corresponding frequency shifts. Cohen *et. al.* [1] considered the case of a fluid electron and kinetic ion response with the Particle-in-Cell (PIC) code BZohar in the small amplitude limit. Because only the ions are trapped, a direct analogy with the trapping of electrons in a driven EPW can be made. The negative frequency shift was shown to scale as expected with $\sqrt{\phi}$, but no attempt was made to distinguish between adiabatic or sudden distributions. For phase velocities and wave amplitudes not too large, this kinetic shift, involving a distortion of the particle distribution f_0 from a Maxwell-Boltzmann and scaling as $\sqrt{\phi}$, is larger than fluid non-linear shifts, which are proportional to ϕ^2 and related to harmonic generation.[1, 4, 44, 45] The sign of the kinetic shift is opposite to the sign of the curvature of the velocity distribution, d^2f_0/dv^2 , at the wave’s phase velocity $v_\phi = \omega/k$ and thus negative (resp. positive) if $|v_\phi| > v_{th}$ (resp. $|v_\phi| < v_{th}$). The thermal velocity is defined here as $v_{th} = (T/m)^{1/2}$. Electrons in an EPW and ions in an IAW are trapped in the tail of the distribution and therefore cause a negative shift to the frequency. Electrons in an IAW are however trapped in the bulk and contribute with a positive shift. The net shift in an IAW is thus dependent on ZT_e/T_i as the number of ions trapped is strongly dependent on $v_\phi^2/v_{th,i}^2 \propto ZT_e/T_i$, while the number of trapped electrons is essentially independent of the wave’s phase velocity as $v_\phi^2/v_{the}^2 \propto Zm_e/m_i \ll 1$ (for IAWs one has $v_\phi \sim c_s = \sqrt{Z_iT_e/m_i}$, where c_s is the sound speed).

To our knowledge, verification of the theory of adiabatic and sudden distributions [13, 42, 43] by kinetic simulation has not been done systematically. Nor, it appears, has the positive shift of the frequency from electron trapping along with the negative shift from trapped ions been included in kinetic simulations of driven IAWs. Our objectives in the work presented here are to compute, using Vlasov simulations, the frequency of both EPWs and IAWs in the nonlinear state, its dependence on the method of generation and plasma parameters, and in particular the validity of characterizing the steady-state distributions as adiabatic or sudden. In addition, we present results for IAWs which show that for $ZT_e/T_i > 10$ the positive frequency shift from trapped electrons overcomes the negative ion shift, producing a net positive frequency shift. Furthermore, at wave amplitudes such that $e\phi/T_e \gtrsim 0.03$, the contribution of wave harmonics to the frequency shift must be included

to get quantitative agreement of the theory with the simulation. There are two clear effects of the harmonics: 1.) The direct effect on the frequency obtainable from the fluid equations. 2.) The change in the number of trapped particles from the distortion of the waveform away from a sinusoid, which can also affect the kinetic frequency shift. This second effect was confirmed with detailed comparisons of the simulations with theory that involved computing the number of trapped electrons and ions by using the simulation's distributions and the analytic distributions corresponding to the sudden or adiabatic approximations. We indeed find that at larger amplitudes the nonsinusoidal waveforms (from wave harmonics) produced in the simulations must be accounted for in the theory to properly calculate the number of trapped particles. However, the number of trapped particles does not in general permit a clear distinction between adiabatic and sudden distributions, as the difference vanishes for small amplitudes. The final confirmation of our interpretation of frequency shifts comes from computing the distributions of resonant trapped and passing particles as a function of the particle energy. These distributions are very well represented as adiabatic or sudden when compared to theory but, again, the actual waveforms, not a sinusoid, may be required for excellent agreement.

We simulate the non-linear evolution of IAWs by driving the waves with an external traveling wave field over many ion acoustic wave periods. Because of the large ion-to-electron mass ratio, the rate of increase of the wave amplitude will be much less than the electron bounce frequency $\omega_{b,e}$, except for very small amplitudes; that is, if the required time t_{drive} for driving the IAW to a certain amplitude ϕ is such that $\omega_{b,e} t_{\text{drive}} = \sqrt{e\phi/T_e} \sqrt{m_i/Zm_e} \omega_a t_{\text{drive}} \gg 1$, with $\omega_a = kc_s$ the acoustic wave frequency, one expects the electrons to respond adiabatically. The ion bounce frequency is however less than ω_a , as $\omega_{b,i}/\omega_a = \sqrt{e\phi/T_e} < 1$, so that one expects the ions to respond adiabatically only if $\omega_a t_{\text{drive}} \gg 1$.

The frequency in the non-linear state is found as a function of wave amplitude, with ZT_e/T_i a key parameter. For $ZT_e/T_i \gg 10$, only electron kinetic effects are important and the non-linear frequency increases with wave amplitude in accord with an adiabatic electron distribution. However, when the trapping width $\Delta v_{\text{tr}} = 2\sqrt{e\phi_0/m_e}$ in velocity space exceeds $\sim v_{\text{th},e}/4$, the number of trapped electrons is less than for an adiabatic or a sudden distribution with a purely sinusoidal wave. Using for the theoretical estimate the actual wave field $\phi(x, t)$ from the simulation, we find excellent agreement with the simulated number of trapped electrons. The adiabatic limit works equally well for representing the

electron distribution for all values of ZT_e/T_i . For $ZT_e/T_i \leq 10$, a significant number of ions are trapped and act to decrease the frequency in the non-linear state. We find in this case that the analytic approximations for the non-linear frequency shifts are sensitive to the choice of the linear frequency estimate ω_L , about which the non-linear dielectric function is expanded, as the number of trapped ions is exponentially dependent on $v_\phi/v_{th,i}$. For finite $k\lambda_{De}$, the estimate for ω_L obtained from a fluid dispersion relation overestimates the contribution from the ions. Here, $\lambda_{De} = v_{th,e}/\omega_{pe}$ is the electron Debye length. For $ZT_e/T_i = 10$, we find that the ions are best represented by an adiabatic distribution with the agreement being particularly good at large amplitude. Again, the actual waveform is required to get good agreement between the simulated ion distribution and the analytic one. When $ZT_e/T_i = 6$, the ions dominate the frequency shift in the non-linear state, and the sudden approximation is the best representation of the non-linear state of the ion distribution.

For completeness, we also analyze the non-linear evolution of EPWs from an initially large amplitude wave or by driving the wave with an external traveling wave potential. The waves evolve to an undamped BGK-like state with a frequency that decreases with wave amplitude with a proportionality constant that depends on the generation process, initialized or slowly-driven, which we again compare to the two analytic limits, sudden or adiabatic. Lindberg [12] also considered the properties of adiabatically driven EPWs, comparing his theoretical estimates to Vlasov simulations, as well as to previous results, in particular with respect to frequency shifts. In the limit of small amplitude, $e\phi/T_e \ll 1$, he confirmed the theoretical results for the coefficient of frequency shift for adiabatic excitation of EPWs considered by Dewar [43] and Benisti [28]. In the same small amplitude limit, other authors [21, 46, 47] had obtained different coefficients. Our simulation results support the coefficients obtained by Dewar in the appropriate limits.

Despite the tremendous growth of computer resources, fluid modeling of the evolution of the driven electrostatic waves with models of kinetic effects [7, 8, 13, 14, 23, 31] is of great practical interest, as fully kinetic simulations of laser propagation through plasmas that account for the actual laser beam size and plasma volume are still not yet accessible. Fluid models that can reproduce the amplitude and phase history of the fields without following the distributions are an essential step towards including kinetic effects in fully 3D fluid codes [48–50] that model Stimulated Brillouin Scattering (SBS) or Stimulated Raman Scattering

(SRS) in Inertial Confinement Fusion (ICF) experiments. As a first step for modeling driven IAWs with electron kinetic effects, we generalized a single species IAW model [7] and applied it to both electrons and ions. In this model, as the wave traps particles, the contribution from each species to the linear damping rate decreases, while the contribution to the frequency shift grows. The electron response is instantaneous but the ion response is not, in accord with their very different bounce frequencies. The wave growth ceases when the external drive stops or the wave gets out of phase with the drive because of the frequency shift. Overall, there is good agreement between the model's and simulation's wave amplitude history but quantitative differences between the respective frequencies in steady state.

Our work was motivated in part by previous work with kinetic simulations and fluid theory with simple models of wave-amplitude dependent kinetic effects. Our examination of electron kinetic effects on IAWs was preceded by theory predicting a modulational instability for IAWs[51] and by kinetic simulations[2, 3], where the nonlinear response of driven IAWs was shown to be significantly different in the case that both the electrons and ions respond kinetically from the case that only ions do and the electron response is assumed adiabatic. In other previous kinetic studies [5, 6, 9], the saturation of SRS by ion trapping effects in the absence of electron trapping used PIC simulations with a fluid Boltzmann treatment of the electrons. The results of kinetic simulations of SRS [20] have been interpreted as well with theoretical models that require amplitude-dependent frequency shifts. With both PIC simulations and theory, Rose and colleagues [24, 27] showed that this amplitude dependence in two-dimensional systems can cause the EPW to self-focus and saturate stimulated Raman scattering (SRS) by reducing the coherence of the interaction. Similarly, Williams and co-workers [8] used an analytic model with a negative amplitude-dependent frequency shift to show a nonlinear limit to the power transfer of overlapping laser beams in a flowing plasma. Also, the sign of the non-linear frequency shift of IAWs is predicted to affect the nature of the possible decay through modulational instabilities.[4] Thus, a systematic study of the size and sign of the frequency shifts and how they depend on the method of wave generation is of clear practical interest.

This paper is organized as follows:

A review of the theory of kinetic and fluid non-linear frequency shifts caused by both particle trapping as well as harmonic generation is presented in Sec. II. The general relation for the kinetic shift is given by Eq. (16). The specific results for the frequency shifts for EPWs

and IAWs are derived in Secs. II A and II B. The kinetic shifts are given by Eqs. (19) and (24), while the additional fluid shifts from higher harmonics are given by Eqs. (20) and (34) for EPWs and IAWs respectively. In Sec. III, the SAPRISTI code used for carrying out the Vlasov-Poisson simulations presented in this paper is described for the first time: the simulation model itself is discussed in Sec. III A, the semi-Lagrangian method applied for evolving the Vlasov equation in Sec. III B 1, and the numerical solution to Poisson's Equation in Sec. III B 2. Also, the methods considered for accurately estimating the frequency of the nonlinear wave with the Hilbert transform technique is discussed in Sec. III C.

The simulation results compared to the theoretical predictions for the frequency shifts, the number of trapped particles, and the distribution functions for both sudden and adiabatic wave generation are discussed in Sec. IV for both EPWs and IAWs. The EPW frequency shifts are given in Sec. IV A: for $k\lambda_{De} = 1/3$ in Sec. IV A 1 and for $k\lambda_{De} = 0.425$ in Sec. IV A 2. The simulation results for IAW frequency shifts are shown in Sec. IV B: with the case $ZT_e/T_i = 30$ in Sec. IV C 1, $ZT_e/T_i = 10$ in Sec. IV C 2, and $ZT_e/T_i = 6$ in Sec. IV C 3. The comparison for IAWs of the fraction of trapped particles from the simulations with the theory is given in Sec. IV C: for the case $ZT_e/T_i = 30$ in Sec. IV B 1, $ZT_e/T_i = 10$ in Sec. IV B 2, and $ZT_e/T_i = 6$ in Sec. IV B 3. This simulation section concludes in Sec IV D with a comparison of the IAW distribution function of the resonant particles as a function of particle energy with the theoretically-obtained adiabatic and sudden distributions. The IAW example shows unambiguous identification of the electron and ion distributions as adiabatic in the particular case $ZT_e/T_i = 10$.

A simple *ad hoc* fluid model that reproduces the essential features of the driven kinetic simulations, *e.g.* a reduction in damping accompanied by a frequency shift that detunes the wave from the driving potential, is presented in Sec. V. We conclude in Sec. VI where we also discuss briefly the detrapping mechanisms of transverse loss and of collisions, which can potentially interfere with the resonant wave-particle interaction and thus affect the resulting frequency shifts. More detailed estimates of collisional effects are presented in the Appendix A.

II. ANALYTIC DERIVATION OF NON-LINEAR FREQUENCY SHIFTS RESULTING FROM RESONANT WAVE-PARTICLE INTERACTION AND HARMONIC GENERATION

In this section, the derivation of the non-linear frequency shift of electrostatic waves resulting from resonant wave-particle interaction (in particular trapping), as originally presented by Morales & O’Neil [42] and Dewar [43], is summarized before being applied to both the case of EPWs as well as of IAWs including non-adiabatic electron effects. We also recall the estimate obtained in previous work, using a fluid representation, for the frequency shift of an EPW resulting from non-linear harmonic generation [44] and derive a similar estimate for IAWs.

Let us start by briefly recalling the general derivation of the non-linear kinetic frequency shift of an electrostatic plasma wave resulting from resonant wave-particle interaction, as originally presented in Refs. [42, 43]. One assumes the plane wave to be propagating along the x direction. The starting point is Poisson’s equation for the potential $\phi(x, t)$ of the final state of the wave:

$$\frac{d^2\phi}{dx^2} = -\frac{1}{\epsilon_0} \sum_{\text{species}} q \int_{-\infty}^{+\infty} dv f, \quad (1)$$

where $f(x, v, t)$ is the time asymptotic distribution in the x -direction (v is the velocity along x) for each species of mass m and charge q . At this point, both the potential ϕ and distribution f are considered in the lab frame. In the following, one shall assume that the wave is an undamped BGK-like mode [40], which is essentially sinusoidal, *i.e.* $\phi(x, t) = \phi_0 \cos(kx - \omega t)$ with amplitude ϕ_0 , wave number k , and frequency ω .

To isolate the purely non-linear response, one adds and subtracts in Eq. (1) the charge density related to the linear response of the system:

$$\begin{aligned} \frac{d^2\phi}{dx^2} &= -\frac{1}{\epsilon_0} \sum_{\text{species}} q \left[\int_{-\infty}^{+\infty} dv f_L + \int_{-\infty}^{+\infty} dv (f - f_L) \right] \\ &= -\frac{1}{\epsilon_0} \sum_{\text{species}} q \left[\int_{-\infty}^{+\infty} dv \delta f + \int_{-\infty}^{+\infty} dv \Delta f_{\text{NL}} \right], \end{aligned} \quad (2)$$

where for each species one defines the non-linear deviation $\Delta f_{\text{NL}} = f - f_L$ of the full distribution f from the linear response $f_L = f_0 + \delta f$, δf being the actual linear perturbation. In Eq. (2) one made use of the fact that the initial unperturbed distributions f_0 verify the neutrality condition $\sum_{\text{species}} q \int dv f_0 = 0$.

From the linearized Vlasov equation:

$$\frac{\partial \delta f}{\partial t} + v \frac{\partial \delta f}{\partial x} - \frac{q}{m} \frac{\partial \phi}{\partial x} \frac{\partial f_0}{\partial v} = 0,$$

one derives δf in the lab frame:

$$\delta f = \frac{q}{m} \frac{k\phi}{kv - \omega} \frac{\partial f_0}{\partial v}. \quad (3)$$

Inserting Eq. (3) into Eq. (2) one can write:

$$k^2 \epsilon_L(k, \omega) \phi = \frac{\Delta \rho_{\text{NL}}}{\epsilon_0}. \quad (4)$$

On the left hand side of Eq. (4), ϵ_L is the linear, kinetic dielectric function given by

$$\epsilon_L(k, \omega) = 1 - \sum_{\text{species}} \frac{\omega_p^2}{k^2} \int dv \frac{\frac{\partial f_0/N}{\partial v}}{v - \omega/k}, \quad (5)$$

with $\omega_p = \sqrt{Nq^2/m\epsilon_0}$ the plasma frequency and N the unperturbed density of each species. On the right hand side of Eq. (4), $\Delta \rho_{\text{NL}}$ stands for the charge separation due to non-linear effects:

$$\Delta \rho_{\text{NL}} = \sum_{\text{species}} q \int_{-\infty}^{+\infty} dv \Delta f_{\text{NL}}.$$

Carrying out the projection $(1/\lambda) \int_{-\lambda/2}^{\lambda/2} dx \phi \dots$ on each side of Eq. (4) gives:

$$\epsilon_{\text{NL}}(k, \omega; \phi_0) = \epsilon_L(k, \omega) + \sum_{\text{species}} \Delta \epsilon_{\text{NL}} = 0, \quad (6)$$

where $\epsilon_{\text{NL}}(k, \omega, \phi_0)$ stands for the non-linear dielectric function and having defined

$$\Delta \epsilon_{\text{NL}} = -\frac{2}{\epsilon_0 E_0^2} \frac{1}{\lambda} \int_{-\lambda/2}^{\lambda/2} dx q \phi \int_{-\infty}^{+\infty} dv \Delta f_{\text{NL}}, \quad (7)$$

$\lambda = 2\pi/k$ being the wavelength and $E_0 = k\phi_0$ the amplitude of the electrostatic wave field. The term $\Delta \epsilon_{\text{NL}}$ can be viewed as the non-linear correction from each species to the kinetic dispersion relation.

The non-linear frequency shift is defined as $\delta\omega_{\text{NL}} = \omega - \omega_L$, where ω_L is the linear frequency related to the wave number k . The frequency ω_L thus verifies the linear dispersion relation:

$$\epsilon_L(k, \omega_L) = 0.$$

Assuming the shift $\delta\omega_{\text{NL}}$ is sufficiently small, it can be derived explicitly from Eq. (6) by expanding its left hand side in a Taylor series with respect to ω :

$$\epsilon_{\text{L}}(\omega = \omega_{\text{L}} + \delta\omega_{\text{NL}}) = \frac{\partial\epsilon_{\text{L}}(\omega_{\text{L}})}{\partial\omega} \delta\omega_{\text{NL}} + \dots = - \sum_{\text{species}} \Delta\epsilon_{\text{NL}},$$

which leads to

$$\delta\omega_{\text{NL}} \simeq - \left[\frac{\partial\epsilon_{\text{L}}(\omega_{\text{L}})}{\partial\omega} \right]^{-1} \sum_{\text{species}} \Delta\epsilon_{\text{NL}}. \quad (8)$$

The main problem in estimating the shift $\delta\omega_{\text{NL}}$ thus involves computing $\Delta\epsilon_{\text{NL}}$, which in turn hinges on specifying the non-linear distribution f .

To derive an explicit relation for f , one makes use of the assumption that the system reached a stationary state in the wave frame. In the following until mentioned otherwise, all physical quantities are now measured from this reference frame, in particular the phase space variables (x, v) as well as the fields ϕ and f . The distribution f , solution to the Vlasov equation, thus becomes a function of the constants of motion: Energy $W = mv^2/2 + q\phi(x)$ and, for passing particles only, the sign $\sigma = \text{sgn}(v)$ of the velocity along x . The distribution $f(W, \sigma)$ is in fact not uniquely defined and depends on how the wave was generated. Two limiting cases have been considered by Dewar[43]:

1. **Sudden:** In this case, the initial distribution f_0 is subjected instantly to the finite amplitude field ϕ , and filaments as a result of the difference in trajectory periods for neighboring energy levels W and $W + \delta W$. Coarse-graining over this filamentation and invoking the invariance of the distribution along the trajectories, the final distribution f is thus effectively given by the average of the initial distribution $f_0(v)$ over the phase space region defined by the energy interval $[W, W + \delta W]$ (see Fig. 1):

$$\sum_{\sigma=\pm 1} f(W, \sigma) = \frac{\sum_{\sigma} \langle f_0[\sigma u(x, W)] \frac{H(W - q\phi)}{u(x, W)} \rangle_x}{\langle \frac{H(W - q\phi)}{u(x, W)} \rangle_x}, \quad (9)$$

where $H(w)$ is the Heaviside function and $u(x, W) = +[(2/m)(W - q\phi(x))]^{1/2}$ is the (positive) velocity at x for the phase space orbit corresponding to the energy level W . The notation $\langle A \rangle_x = (1/\lambda) \int_{-\lambda/2}^{\lambda/2} dx A(x)$ stands for the average along x of quantity A .

2. **Adiabatic:** One assumes the wave to be driven up sufficiently slowly such that one may invoke the adiabatic invariant $\int dx v$, where the integral is carried out over one bounce period for trapped particles and one wavelength for passing particles. Further

making use again of the invariance of the distribution along the particle trajectory, one obtains:

$$\sum_{\sigma=\pm 1} f(W, \sigma) = \sum_{\sigma=\pm 1} f_0(\sigma \bar{u}), \quad (10)$$

with $\bar{u}(W) = \langle u(x, W) H(W - q\phi) \rangle_x$.

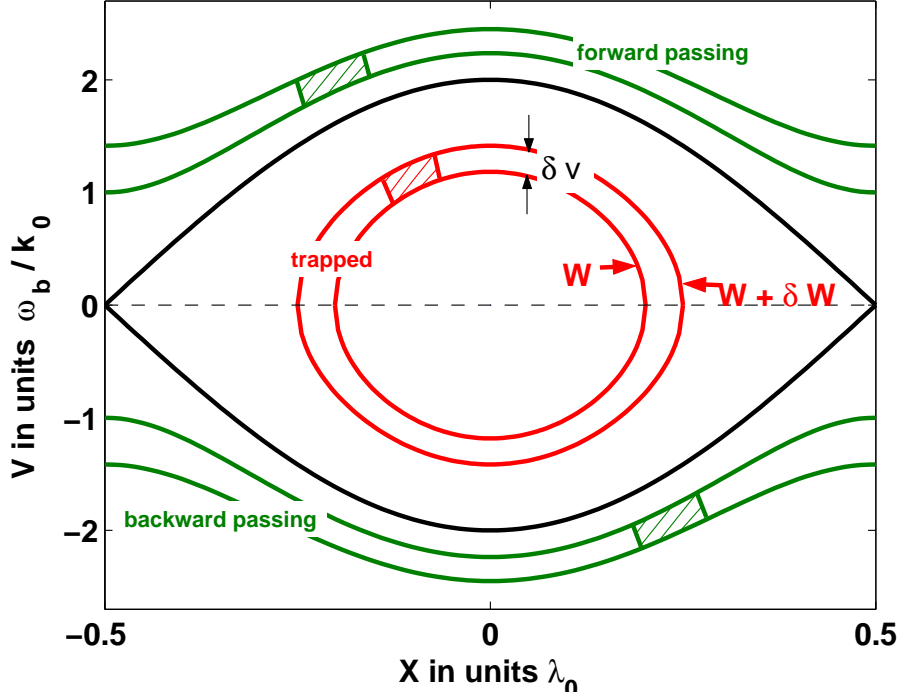


FIG. 1: (color online) Distribution in resonant region seen from the wave frame. Phase space trajectories corresponding to two neighboring energy levels W and $W + \delta W$ are shown in the trapped (red) as well as in the forward ($\sigma = \text{sgn}(v) > 0$) and backward ($\sigma < 0$) passing regions (green). Corresponding small phase space volumes (dashed), which undergo filamentation over time in the sudden case, are also pointed out. The separatrix (black), given by $\pm u(x, W = |q|\phi_0)$, delimits the trapping from the passing regions.

The wave amplitude is assumed sufficiently small such that the bulk still responds linearly, the only non-linear effect resulting from the resonant particles. The non-linear deviation Δf_{NL} is thus essentially non-zero in the resonant region. For computing Δf_{NL} one thus evaluates the distributions (3), (9), and (10) by Taylor-expanding f_0 to second order around $v = 0$:

$$f_0(v) = f_0(0) + \frac{df_0(0)}{dv}v + \frac{1}{2}\frac{d^2f_0(0)}{dv^2}v^2 + \dots \quad (11)$$

Together with the assumption of a sinusoidal wave, written as $\phi = \phi_0 \cos(kx)$ in the wave frame, the so-obtained relations for Δf_{NL} (for both the sudden and the adiabatic case) are then inserted into Eq. (7), which leads to:

$$\Delta \epsilon_{\text{NL}} = \alpha \frac{\omega_p^2}{k^2} \Delta v_{\text{tr}} \left. \frac{d^2(f_0/N)}{dv^2} \right|_{v_\phi}, \quad (12)$$

where $\Delta v_{\text{tr}} = 2(|q|\phi_0/m)^{1/2}$ is the trapping width for each species. In Eq. (12), the equilibrium distribution f_0 has again been written in the lab frame and for a Maxwellian distribution:

$$\frac{d^2(f_0/N)}{dv^2} = \frac{1}{\sqrt{2\pi}} \frac{1}{v_{\text{th}}^3} [(v/v_{\text{th}})^2 - 1] \exp \left[-\frac{1}{2}(v/v_{\text{th}})^2 \right]. \quad (13)$$

The coefficient α in Eq. (12) can be expressed in terms of $F(\kappa^2) = \int_0^{\pi/2} d\theta / (1 - \kappa^2 \sin^2 \theta)^{1/2}$ and $E(\kappa^2) = \int_0^{\pi/2} d\theta (1 - \kappa^2 \sin^2 \theta)^{1/2}$, *i.e.* the complete elliptic integrals of first and second kind respectively with argument $\kappa^2 = 2|q|\phi_0/(W + |q|\phi_0)$ being a normalized energy variable, providing the following relations for both the “sudden” and the “adiabatic” cases:

1. Sudden wave generation:

$$\begin{aligned} \alpha &= \frac{8}{\pi} \int_0^1 d\kappa \left\{ \underbrace{\frac{1}{\kappa^6 F} [2(F - E) - \kappa^2 F]^2}_{\text{resonant passing}} + \underbrace{\frac{\kappa}{F} (F - 2E)^2}_{\text{trapped}} \right\} \\ &= 0.117 + 0.705 = 0.823, \end{aligned} \quad (14)$$

2. Adiabatic wave generation:

$$\begin{aligned} \alpha &= \frac{16}{\pi} \int_0^1 d\kappa \left\{ \underbrace{\frac{1}{\kappa^4} \left[\left(\frac{1}{\kappa^2} - \frac{1}{2} \right) - \frac{4}{\pi^2 \kappa^2} E^2 \right] [2(F - E) - \kappa^2 F]}_{\text{resonant passing}} \right. \\ &\quad \left. + \underbrace{\kappa \left[\left(\kappa^2 - \frac{1}{2} \right) - \frac{4}{\pi^2} ((\kappa^2 - 1)F + E)^2 \right] (F - 2E)}_{\text{trapped}} \right\} \\ &= 0.052 + 0.493 = 0.544. \end{aligned} \quad (15)$$

The above values have been obtained by numerical integration and make explicit the separate contributions from resonant passing and trapped particles. Note, the non-linear kinetic

frequency shifts do not result from trapped particles alone, as resonant passing particles, i.e. with velocity close to v_ϕ , contribute as well. The contributions from trapped particles dominate however over the ones from resonant passing in the proportions 86%/14% for the sudden case, and 90%/10% for the adiabatic case. Note also that the total shift for the sudden case is larger by $\sim 50\%$ compared to the adiabatic scenario.

Combining Eqs. (8) and (12) finally leads to the effective analytic relation for the frequency shift:

$$\delta\omega_{\text{NL}} \simeq - \left[\frac{\partial\epsilon_L(\omega_L)}{\partial\omega} \right]^{-1} \sum_{\text{species}} \alpha \frac{\omega_p^2}{k^2} \Delta v_{\text{tr}} \left. \frac{d^2(f_0/N)}{dv^2} \right|_{v_\phi}. \quad (16)$$

One can deduce from this relation, that the sign of the contribution to the frequency shift from each species depends on both the sign of $\partial\epsilon_L/\partial\omega$ (independent of species) at the frequency ω_L of the wave, as well as on the curvature of the particle's initial distribution f_0 at the phase velocity v_ϕ . Let us point out that it is essential to fix the sign of ω_L to clearly specify the sign of the frequency shifts. The frequency ω_L is thus chosen to be positive. With this convention, $\partial\epsilon_L/\partial\omega$ is in fact positive for both EPWs and IAWs, as will be shown by Eqs. (18) and (23). The sign of the frequency shift contribution from each species is therefore opposite to the sign of $d^2(f_0/N)/dv^2|_{v_\phi}$, which for a Maxwellian distribution, according to Eq. (13), is thus positive if $|v_\phi| < v_{\text{th}}$ and negative if $|v_\phi| > v_{\text{th}}$.

In the following, as a reminder, we shall first apply Eq. (16) to the case of an electron plasma wave before applying this relation to the case of an ion acoustic wave.

A. Non-Linear Frequency Shifts for EPWs

In this case, due to the high frequency of the EPWs, and the small electron to ion mass ratio, only electron dynamics need to be considered. Including lowest order thermal corrections, the dielectric function is given by

$$\epsilon_L(k, \omega) = 1 - \frac{\omega_{pe}^2}{\omega^2} - 3 \frac{\omega_{pe}^2}{\omega^2} \left(\frac{kv_{\text{th,e}}}{\omega} \right)^2,$$

Solving the dispersion relation $\epsilon_L(k, \omega_L) = 0$, one then obtains the Bohm-Gross relation for the linear frequency, valid for $k\lambda_{De} \ll 1$:

$$\omega_L^2 = \omega_{pe}^2 + 3(kv_{\text{th,e}})^2. \quad (17)$$

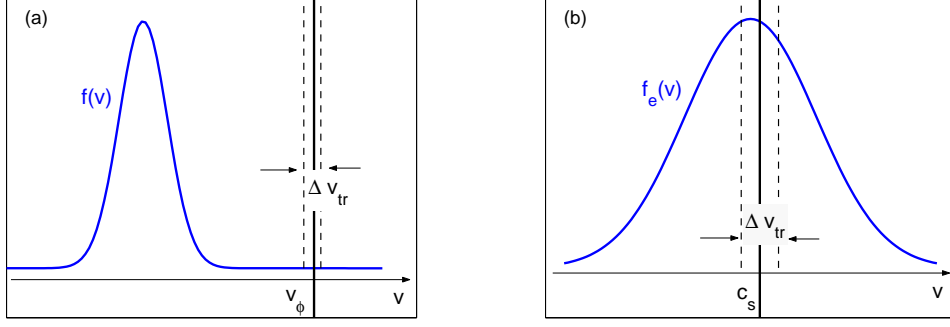


FIG. 2: (color online) a) Electrons in an EPW or ions in an IAW: trapping in tail of distribution. b) Electrons in an IAW: trapping in bulk of distribution.

For estimating $\partial\epsilon_L(\omega_L)/\partial\omega$ one neglects thermal effects, so that the dielectric function is approximated by $\epsilon_L \simeq 1 - \omega_{pe}^2/\omega^2$, thus providing $\omega_L \simeq \omega_{pe}$ and

$$\frac{\partial\epsilon_L(\omega_L)}{\partial\omega} \simeq 2/\omega_{pe}. \quad (18)$$

Invoking Poisson's equation, one can also express the trapping width in terms of the electron density perturbation amplitude δN_e :

$$\frac{\Delta v_{tr}}{v_{th,e}} = 2 \left(\frac{e\phi}{T_e} \right)^{1/2} = \frac{2}{k\lambda_{De}} \left(\frac{\delta N_e}{N_e} \right)^{1/2},$$

where $\lambda_{De} = v_{th,e}/\omega_{pe}$ is the electron Debye length. From Eqs. (13) and (16), the non-linear frequency shift due to resonant electrons in an EPW then becomes:

$$\frac{\delta\omega_{NL}}{\omega_{pe}} = -\frac{\alpha_e}{(k\lambda_{De})^3} \left(\frac{\delta N_e}{N_e} \right)^{1/2} \frac{1}{\sqrt{2\pi}} (v^2 - 1) \exp\left(-\frac{v^2}{2}\right) \Big|_{v=v_\phi/v_{th,e}}, \quad (19)$$

where the more accurate relation (17) for ω_L is used for estimating the argument $v = v_\phi/v_{th,i}$ appearing in the exponential:

$$\frac{v_\phi}{v_{th,e}} = \frac{\omega}{kv_{th,e}} = \left[\frac{1}{(k\lambda_{De})^2} + 3 \right]^{1/2}.$$

The parameter α_e takes on one of the two values given by relations (14) and (15) depending on how the EPW was generated. Note that in this case $\delta\omega_{NL}$ is negative as $v_\phi/v_{th,e} \simeq 1/(k\lambda_{De}) \gg 1$. A cartoon pointing out the trapping around v_ϕ of electrons in an EPW in the tail of the distribution is shown in Fig. 2.a.

In addition to this negative kinetic shift, a positive shift of the EPW frequency resulting from non-linear wave harmonic generation has been obtained in the frame of a fluid representation:[44]

$$\frac{\delta\omega_{\text{harm}}}{\omega_{pe}} = \frac{1}{4\sqrt{1+3\tilde{k}^2}} \left(15\tilde{k}^6 + 48\tilde{k}^8\right) \tilde{\phi}^2, \quad (20)$$

where $\tilde{k} = k\lambda_{De}$ and $\tilde{\phi} = e\phi/T_e$. As will be shown in Sec. IV A, for the parameters considered for EPWs in this paper, the kinetic shift, scaling as $\sqrt{\phi}$, dominates the fluid harmonic shift, scaling as ϕ^2 .

B. Non-Linear Frequency Shifts for IAWs

As will be shown in Sec. IV B, for all considered wave amplitudes, the dominant contribution to the frequency shift of IAWs comes from the interaction with resonant electrons and ions. For $e\phi/T_e \gtrsim .03$, the IAWs nonetheless develop significant 2nd harmonic content that causes an additional frequency shift derivable from the isothermal, cold-ion fluid equations, which is the subject of Sec. II B 2. First, the larger kinetic shifts are discussed.

1. IAW Frequency Shift from Resonant Electron and Ion Wave Interaction

Here, both electron and ion dynamics contribute. For a first estimation, one approximates the dielectric function in the case of IAWs by

$$\epsilon_L \simeq 1 + \frac{1}{(k\lambda_{De})^2} - \frac{\omega_{pi}^2}{\omega^2} - 3\frac{\omega_{pi}^2}{\omega^2} \left(\frac{kv_{\text{th},i}}{\omega}\right)^2, \quad (21)$$

i.e. including adiabatic electron response and lowest order thermal corrections for ions. Solving the corresponding linear dispersion relation $\epsilon_L(\omega_L) = 0$ provides the linear frequency

$$\omega_L = |k| c_s \left[\frac{1}{1 + (k\lambda_{De})^2} + 3\frac{T_i}{Z T_e} \right]^{1/2}, \quad (22)$$

where $c_s = (ZT_e/m_i)^{1/2}$ is the sound speed and Z the ionization degree of ions. Neglecting finite $k\lambda_{De}$ (charge separation) and T_i/ZT_e effects, so that $\omega_L \simeq |k| c_s$, one also estimates

$$\frac{\partial\epsilon_L(\omega_L)}{\partial\omega} \simeq \frac{2\omega_{pi}^2}{(|k|c_s)^3}. \quad (23)$$

Based on the linearized adiabatic response of the bulk electrons, $\delta N_e/N_e = e\phi/T_e$, one can compute the trapping widths for both electrons and ions:

$$\begin{aligned}\frac{\Delta v_{\text{tr},e}}{v_{\text{th},e}} &= 2 \left(\frac{e\phi}{T_e} \right)^{1/2} = 2 \left(\frac{\delta N_e}{N_e} \right)^{1/2}, \\ \frac{\Delta v_{\text{tr},i}}{v_{\text{th},i}} &= 2 \left(\frac{q\phi}{T_i} \right)^{1/2} = 2 \left(\frac{ZT_e}{T_i} \right)^{1/2} \left(\frac{\delta N_e}{N_e} \right)^{1/2}.\end{aligned}$$

Finally, inserting the above relations into Eq. (16) provides the following frequency shift for IAWs:

$$\frac{\delta\omega}{|k|c_s} = \left(\frac{\delta N_e}{N_e} \right)^{1/2} \frac{1}{\sqrt{2\pi}} \left[\alpha_e - \alpha_i \left(\frac{ZT_e}{T_i} \right)^{3/2} (\mathbf{v}^2 - 1) \exp\left(-\frac{\mathbf{v}^2}{2}\right) \right]_{\mathbf{v}=v_\phi/v_{\text{th},i}}, \quad (24)$$

where the more accurate relation (22) for ω_L is used for estimating the argument $\mathbf{v} = v_\phi/v_{\text{th},i}$ appearing in the exponential:

$$\frac{v_\phi}{v_{\text{th},i}} = \frac{\omega}{kv_{\text{th},i}} = \left[\frac{ZT_e/T_i}{1 + (k\lambda_{De})^2} + 3 \right]^{1/2}. \quad (25)$$

The first and second terms in Eq. (24) are, respectively, the positive electron and negative ion contributions to the frequency shift. The parameters α_e and α_i again take on one of the values (not necessarily the same) of relations (14) or (15), depending on how the wave was generated. In the case of IAWs, Fig. 2.a illustrates the trapping of ions in the tail of their distribution as the phase velocity is typically such that $|v_\phi| \gg v_{\text{th},i}$, resulting from the assumption $ZT_e/T_i \gg 1$, while Fig. 2.b sketches the trapping of electrons in the bulk of their distribution as $|v_\phi| \ll v_{\text{th},e}$, resulting from $Zm_e/m_i \ll 1$.

From Eq. (24), one can estimate the ratio of the ion to electron contributions to the non-linear frequency shift, assuming here $\alpha_e = \alpha_i$:

$$\left| \frac{\delta\omega_i}{\delta\omega_e} \right| = \left(\frac{ZT_e}{T_i} \right)^{3/2} (\mathbf{v}^2 - 1) \exp\left(-\frac{\mathbf{v}^2}{2}\right)_{\mathbf{v}=v_\phi/v_{\text{th},i}}, \quad (26)$$

with $\mathbf{v} = v_\phi/v_{\text{th},i}$ given by Eq. (25). Relation (26) is plotted in Fig. 3 as a function of ZT_e/T_i . The weaker dependence on $k\lambda_{De}$ is shown by plotting curves for different physically relevant values of this parameter ($0 < k\lambda_{De} < 0.5$). Notice that for high values of ZT_e/T_i , the frequency shift is dominated by the positive electron contribution ($|\delta\omega_i| < |\delta\omega_e|$), while for lower values the negative ion contribution can become competitive or even dominant ($|\delta\omega_i| > |\delta\omega_e|$). One expects that the two contributions cancel each other out near $ZT_e/T_i \simeq 10$. Let us emphasize that the ratio $|\delta\omega_i/\delta\omega_e|$ plotted in Fig. 3 is based on the solution

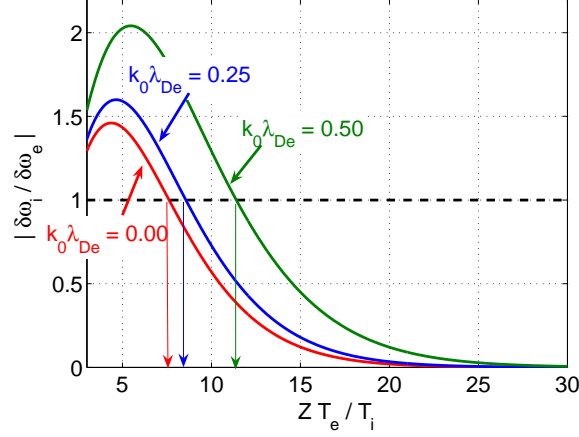


FIG. 3: (color online) Estimate for ratio of ion to electron frequency shift contributions for an IAW. Assuming $\alpha_e = \alpha_i$.

to the dispersion relation $\epsilon_L = 0$ considering the approximate form (21) of the dielectric function ϵ_L , which is only valid in the limit $ZT_e/T_i \gg 1$. The ratios shown in Fig. 3 for $ZT_e/T_i \lesssim 6$ are therefore to be considered as rough estimates only. More accurate values may be obtained using a numerical solution to the dispersion relation with ϵ_L given by the exact form (5), *i.e.* accounting for the complete kinetic response of electrons and ions.

2. IAW Frequency Shift from Harmonic Generation

Here, the frequency shift of an IAW resulting from harmonic generation is derived from the isothermal cold ion fluid equations,

$$\frac{\partial n}{\partial t} + \frac{\partial nv}{\partial x} = 0, \quad (27)$$

$$\frac{\partial v}{\partial t} + v \frac{\partial v}{\partial x} = -\frac{\partial \phi}{\partial x}, \quad (28)$$

$$-\frac{\partial^2 \phi}{\partial x^2} + \exp \phi = n, \quad (29)$$

where density n has been normalized to a uniform background density n_0 , the electrostatic potential ϕ to T_e/e , time t to the inverse of the ion plasma frequency ω_{pi}^{-1} , v to the sound speed $c_s = \sqrt{ZT_e/m_i}$, and position x to the electron Debye length λ_{De} . Following Pesme *et al.*, [4] one expands the variables in a Fourier series:

$$(\phi, n, v) = (\phi_0, n_0, v_0) + \frac{1}{2} \sum_{l \neq 0} (\phi_l, n_l, v_l) \exp[i l (\tilde{k}x - \tilde{\omega}t)],$$

with the reality condition $(\phi_{-l}, n_{-l}, v_{-l}) = (\phi_l, n_l, v_l)^*$ and keeping terms for $l = 0, \pm 1, \pm 2$ up to 2^{nd} order with $\exp \phi \simeq 1 + \phi + \frac{1}{2}\phi^2$. Collecting terms with matching exponents in the Fourier series, one finds from Eqs. (27)-(29) for $l = 0$:

$$1 + \phi_0 + \frac{\phi_0^2}{2} + \frac{|\phi_1|^2}{4} + \frac{|\phi_2|^2}{4} = n_0, \quad (30)$$

as well as the conditions $v_0 = 0$ and $n_0 = 1$. By conservation of electron number, it thus follows from Eq. (30) that,

$$\phi_0 + \frac{\phi_0^2}{2} = -\frac{|\phi_1|^2}{4} - \frac{|\phi_2|^2}{4}.$$

The equations for $l = 1$ are:

$$\begin{aligned} -i\tilde{\omega}n_1 + i\tilde{k}v_1 + i\frac{\tilde{k}}{2}n_{-1}v_2 + i\frac{\tilde{k}}{2}n_2v_{-1} &= 0, \\ -i\tilde{\omega}v_1 + i\frac{\tilde{k}}{2}v_{-1}v_2 &= -i\tilde{k}\phi_1, \\ (1 + \tilde{k}^2 + \phi_0)\phi_1 &= n_1 - \frac{1}{2}\phi_2\phi_{-1}, \end{aligned}$$

and the corresponding equations for $l = 2$ are:

$$\begin{aligned} -2i\tilde{\omega}n_2 + 2i\tilde{k}v_2 + i\tilde{k}n_1v_1 &= 0, \\ -2i\tilde{\omega}v_2 &= -2i\tilde{k}(\phi_2 + \frac{1}{4}v_1^2), \\ (1 + 4\tilde{k}^2 + \phi_0)\phi_2 + \frac{1}{4}\phi_1^2 &= n_2. \end{aligned}$$

Defining $C_{sl}^2 = l^2\tilde{k}^2/(1 + l^2\tilde{k}^2)$ and keeping terms only to second order in ϕ_1 , one obtains for ϕ_2 the relation,

$$\phi_2 = A_{2\phi}\phi_1^2, \quad A_{2\phi} \equiv \frac{C_{s2}^2}{(4\tilde{\omega}^2 - C_{s2}^2)} \left[-\frac{\tilde{\omega}^2}{4\tilde{k}^2} + \frac{\tilde{k}^2}{4\tilde{\omega}^2} + \frac{1}{2}(1 + \tilde{k}^2) \right]. \quad (31)$$

Retaining harmonic corrections to the linear dispersion relation again up to second order in ϕ_1 (here equivalent to $\phi_0 \simeq -|\phi_1|^2/4$), the following nonlinear equation for the amplitude of ϕ_1 is obtained:

$$(\tilde{\omega}^2 - C_{s1}^2)\phi_1 = (A_{2\phi}C_{A_{2\phi}} + C_2) |\phi_1|^2\phi_1, \quad (32)$$

where

$$\begin{aligned} C_{A_{2\phi}} &\equiv \frac{C_{s1}^2}{2} \left[-\frac{\tilde{\omega}^2}{\tilde{k}^2} + 2\frac{\tilde{k}^2}{\tilde{\omega}^2} + (1 + \tilde{k}^2) \right], \\ C_2 &\equiv \frac{C_{s1}^2}{8} \left[2\frac{\tilde{k}^4}{\tilde{\omega}^4} + 3(1 + \tilde{k}^2)\frac{\tilde{k}^2}{\tilde{\omega}^2} \right] + \frac{\tilde{\omega}^2}{4(1 + \tilde{k}^2)}. \end{aligned}$$

Let $\tilde{\omega}_{\text{harm}} = \tilde{\omega} + \delta\tilde{\omega}_{\text{harm}}$ and $\tilde{\omega}^2 - C_{s1}^2 = 0$, where $\tilde{\omega}_{\text{harm}}$ is the effective fundamental IAW frequency after accounting for harmonic effects. One finds that the frequency shift of the first harmonic due to the inclusion of second harmonic terms is given to second order in ϕ_1 by,

$$\frac{\delta\tilde{\omega}_{\text{harm}}}{\tilde{\omega}} = \frac{1}{2} \frac{\Delta}{\tilde{\omega}^2} |\phi_1|^2, \quad \Delta \equiv A_{2\phi} C_{A_{2\phi}} + C_2. \quad (33)$$

Using the dispersion relation $\tilde{\omega}^2 \simeq \tilde{k}^2/(1 + \tilde{k}^2)$, one obtains the final result:

$$\frac{\delta\tilde{\omega}_{\text{harm}}}{\tilde{\omega}} = \frac{1}{48\tilde{k}^2(1 + \tilde{k}^2)} \left(4 + 45\tilde{k}^2 + 93\tilde{k}^4 + 81\tilde{k}^6 + 24\tilde{k}^8 \right) |\phi_1|^2. \quad (34)$$

Note that the contribution of ϕ_2 decreases with increasing $k\lambda_{De}$ as the second harmonic becomes less resonant since $4\tilde{\omega}^2 - C_{s2}^2 = 4C_{s1}^2 - C_{s2}^2$ increases strongly with $k\lambda_{De}$. Note that Eq. (34) can also be derived using the same type of derivation as considered by Winjum [44] to obtain the fluid non-linear frequency shift (20) for EPWs.

III. VLASOV SIMULATION MODEL, NUMERICAL IMPLEMENTATION, AND ANALYSIS METHODS

The theoretical estimates for the non-linear frequency shifts presented in Sec. II have been compared against simulation results obtained using the SAPRISTI code[52], originally developed to study Stimulated Raman Scattering (SRS) in laser plasma interaction conditions[22]. This code has been more recently generalized to include multi-species, and can now also be run on a parallel platform that makes possible simulation of large systems and/or multiple time scales that are encountered when considering both electron and ion dynamics.

A. Simulation Model

For the results presented in this paper, one considers a one-dimensional, periodic system along x . The system length L is typically chosen one wavelength long: $L = 2\pi/k$, where k is the wavenumber of interest. The non-linear, kinetic dynamics in the presence of an electrostatic wave (EPW or IAW) propagating parallel to x is characterized by the evolution of the distribution $f(x, v, t)$ for each considered species (electrons and/or ions), where v is

the velocity along x . This evolution is described by the Vlasov equation:

$$\frac{D}{Dt} f(x, v, t) \doteq \left[\frac{\partial}{\partial t} + v \frac{\partial}{\partial x} + \frac{q}{m} E_{\text{es}} \frac{\partial}{\partial v} \right] f = 0, \quad (35)$$

where D/Dt stands for the total time derivative along the non-linear trajectories in phase space (x, v) , while $E_{\text{es}} = E_{\text{es}}^{\text{int}} + E_{\text{es}}^{\text{ext}}$ represents the total (longitudinal) electrostatic field, the superposition of the self-consistent, internal component $E_{\text{es}}^{\text{int}}(x, t)$ related to the plasma wave and of an external component $E_{\text{es}}^{\text{ext}}(x, t)$ acting as a driver.

For the initial distribution $f(x, v, t = 0)$, one typically considers the following functional form for each species:

$$f(x, v, t = 0) = \left[1 + \frac{\delta N}{N} \cos(kx) \right] f_0(v), \quad (36)$$

where $\delta N/N$ represents the relative amplitude of a sinusoidal, initial density perturbation with wavenumber k . For the simulations presented in this paper, the initial velocity distribution $f_0(v)$ is chosen to be Maxwellian:

$$f_0(v) = \frac{N}{\sqrt{2\pi} v_{\text{th}}} \exp \left[-\frac{1}{2} \left(\frac{v}{v_{\text{th}}} \right)^2 \right],$$

where N is the background density, $v_{\text{th}} = \sqrt{T/m}$ the thermal velocity, and T the initial temperature.

The self-consistent field $E_{\text{es}}^{\text{int}}$ derives from the electrostatic potential $\phi(x, t)$, which itself is solution to Poisson's equation:

$$\begin{aligned} E_{\text{es}}^{\text{int}} &= -\partial\phi/\partial x, \\ -\frac{\partial^2\phi}{\partial x^2} &= \frac{1}{\epsilon_0} \sum_{\text{species}} q n(x, t), \end{aligned} \quad (37)$$

where the total density field n of each species is computed from its distribution:

$$n(x, t) = \int_{-\infty}^{+\infty} dv f(x, v, t).$$

Initial distributions of the form (36) with non-zero δN give rise to stationary waves. Alternatively, starting with $\delta N = 0$, the external field $E_{\text{es}}^{\text{ext}}$ provides a practical way to drive the system and generate propagating waves. This field emulates the ponderomotive drive arising from the beating of the incident and scattered light in SRS or SBS. To generate a given propagating wave, one thus considers

$$E_{\text{es}}^{\text{ext}}(x, t) = E_0^{\text{ext}}(t) \cos(kx - \omega^{\text{ext}}t), \quad (38)$$

where k is the wavenumber of the wave one intends to drive and ω^{ext} is chosen in the vicinity of the corresponding estimated linear frequency ω_L . The external drive can be individually turned on or off for the different species. Furthermore, the driver amplitude $E_0^{\text{ext}}(t)$ is usually smoothly ramped up over an initial time interval t_{ramp} from essentially zero to a value E_0^{ext} , where it is kept constant until a time $t_{\text{stop}} = t_{\text{ramp}} + t_{\text{drive}}$, after which it is ramped down to zero, again over a time interval of length t_{ramp} . Such a modulation of the external drive allows generation of waves which are freely propagating after the time $t_{\text{stop}} + t_{\text{ramp}}$. The functional form of $E_0^{\text{ext}}(t)$ is thus chosen of the form

$$\frac{E_0^{\text{ext}}(t)}{E_0^{\text{ext}}} = \frac{1}{2} \left\{ \tanh \left[R \left(\frac{2t}{t_{\text{ramp}}} - 1 \right) \right] - \tanh \left[R \left(\frac{2(t - t_{\text{stop}})}{t_{\text{ramp}}} - 1 \right) \right] \right\}. \quad (39)$$

Assuming $t_{\text{ramp}} \ll t_{\text{stop}}$, the constant R appearing within the arguments of the tanh functions in Eq. (39) ensures a ramp up of $E_0^{\text{ext}}(t)/E_0^{\text{ext}}$ over the time interval t_{ramp} between ϵ and $1 - \epsilon$ (resp. ramp down between $1 - \epsilon$ and ϵ), where $\epsilon = (1 - \tanh R)/2$. Typically $R = 4$ is chosen, providing $\epsilon = 3.4 \cdot 10^{-4}$.

B. Numerical Implementation

1. The Semi-Lagrangian Method for Solving the Vlasov Equation

The Vlasov equation for the longitudinal dynamics is solved numerically by applying the semi-Lagrangian advection scheme. This method was first considered for evolving the Vlasov equation by Cheng and Knorr [53] and since has been widely applied to low-dimensional kinetic plasma simulations [54–58]. In the SAPRISTI code, this algorithm evolves the particle distribution $f(x, v, t)$ in the longitudinal phase space on a fixed Cartesian mesh, (x_i, v_j) , $i = 0, \dots, I$, $j = 0, \dots, J$, *i.e.* makes use of an Eulerian description, and thus avoids the numerical noise affecting particle in cell (PIC) -type approaches, as considered for example in references [1, 5, 9, 20, 27, 45]. Such an Eulerian scheme thus provides very “clean” simulations, which are straightforward to diagnose. The absence of numerical fluctuations is of particular interest for accurate resolution of the sparsely populated tails when the particle resonantly interacts with a small amplitude wave whose the phase velocity v_ϕ is significantly larger than the thermal velocity v_{th} of a given species ($|v_\phi| \gg v_{\text{th}}$).

The basic idea of the semi-Lagrangian scheme is to invoke the invariance of the distribution along the particle trajectories as described by the Vlasov equation (35). To update

the distribution at a given phase space grid point, one thus integrates back in time along the particle trajectory up to the previous time step and interpolates the previous state of the distribution at the foot of this trajectory. This scheme has the advantage that it is not subject to a so-called Courant-Friedrichs-Lewy (CFL) stability condition on the time step Δt .

To advance the Vlasov equation over one time interval Δt , for instance from time $t_{n-1/2} = (n - 1/2) \Delta t$ to $t_{n+1/2} = (n + 1/2) \Delta t$, one furthermore makes use of a time splitting procedure, which enables separate treatment of the advection along the x and v directions. This amounts to replacing the force field $F(x, t) = (q/m)E_{\text{es}}$ in (35), by the series of impulses:[54]

$$F^*(x, t) = F(x, t) \Delta t \sum_n \delta(t - t_n),$$

where $t_n = n\Delta t$. In the following we shall respectively denote by t_{n-} and t_{n+} the time just prior and just after the impulse at $t = t_n$.

A full time step is carried out as follows:

1. During the time interval $\Delta t/2$ from $t_{n-1/2}$ to t_{n-} , the distribution first undergoes free-streaming, the Vlasov equation reducing to

$$\frac{\partial f}{\partial t} + v \frac{\partial f}{\partial x} = 0, \quad (40)$$

which corresponds to a uniform advection along x with velocity v . In Eq. (40), v thus appears as a parameter and the evolution of the distribution from $t_{n-1/2}$ to t_{n-} can be written

$$f(x, v, t_{n-}) = f(x - v\Delta t/2, v, t_{n-1/2}). \quad (41)$$

This relation simply reflects the invariance of the distribution along the particle trajectory, in this case a uniform motion along x with velocity v .

2. At time t_n , the system undergoes the impulse from F , so that the Vlasov equation reduces to

$$\frac{\partial f}{\partial t} + F(x, t_n) \Delta t \delta(t - t_n) \frac{\partial f}{\partial v} = 0, \quad (42)$$

which now corresponds to an advection along v . Here it is x that appears as a parameter, and the distribution advances as

$$f(x, v, t_{n+}) = f(x, v - F(x, t_n)\Delta t, t_{n-}). \quad (43)$$

3. From time t_{n+} to $t_{n+1/2}$, the main system is again free-streaming, so that

$$f(x, v, t_{n+1/2}) = f(x - v\Delta t/2, v, t_{n+}). \quad (44)$$

It can be shown [53], that the semi-Lagrangian scheme composed of steps 1 to 3 is accurate to second order in time. This requires however that the force field $F(x, t_n)$ be second order accurate as well. This is ensured by appropriately solving the electrostatic field equation, as described in Secs III B 2 and III B 3.

Concerning the phase space discretization, the distribution is represented at a given time by its values $f_{ij} = f(x_i, v_j)$ at the fixed phase space grid points (x_i, v_j) , so that Eqs. (41), (43), and (44) evaluated on this grid become

$$f(x_i, v_j, t_{n-}) = f(x_i - v_j\Delta t/2, v_j, t_{n-1/2}), \quad (45)$$

$$f(x_i, v_j, t_{n+}) = f(x_i, v_j - F(x_i, t_n)\Delta t, t_{n-}), \quad (46)$$

$$f(x_i, v_j, t_{n+1/2}) = f(x_i - v_j\Delta t/2, v_j, t_{n+}). \quad (47)$$

Note that the values $x_i - v_j\Delta t/2$ and $v_j - F(x_i, t_n)\Delta t$ do not in general coincide with any one of the grid points $\{x_i\}$ or $\{v_j\}$ respectively. Computing the right hand sides of relations (45)-(47) thus involves in turn one-dimensional interpolations along the x -direction, the v -direction, and again the x -direction. Such interpolations can be carried out with limited numerical diffusion and dispersion by using cubic spline interpolation [55, 56]. The error related to the cubic spline interpolation is essentially fourth order with respect to the space discretization.

When evaluating the right hand sides of Eqs. (45)-(47), one must also address the issue of the interpolation points (foot of trajectories) falling outside the computation domain $[x_0 = 0, x_I = L] \times [v_0, v_J]$. For Eqs. (45) and (47), related to the advections in x , this involves invoking periodic boundary conditions. More specifically, the feet $x_i - v_j\Delta t/2$ of the trajectories are in fact replaced by $\text{mod}(x_i - v_j\Delta t/2, L)$, where mod stands for the modulo operation.

In case of Eq. (46), dealing with the foot of the trajectory $v_j - F(x_i, t_n)\Delta t$ falling outside the considered velocity domain $[v_0, v_J]$ is somewhat less straightforward, as the original Vlasov equation (35) is defined on an infinite velocity domain $[-\infty, +\infty]$ and thus *a priori* requires no boundary conditions to be specified in this direction. For the numerical system, the lower and upper limits v_0 and v_J of the velocity mesh are chosen so as to ensure that the

distribution is evanescently small at these boundaries, and thus that its evolution becomes essentially independent of the boundary conditions applied in this direction. One typically defines $-v_0 \simeq v_J \simeq 10 v_{\text{th}}$. In the SAPRISTI code, both periodic and open boundaries have in fact been implemented in the v -direction. Periodic boundaries, even though truly unphysical along v , have the advantage of ensuring total mass conservation up to round-off error in case of an equidistant mesh. Open boundaries are implemented as follows:

$$f(x_i, v_j; t_{n+}) = \begin{cases} f(x_i, v_0; t_{n-}) & \text{if } v_j - F(x_i, t_n)\Delta t < v_0, \\ f(x_i, v_J; t_{n-}) & \text{if } v_j - F(x_i, t_n)\Delta t > v_J, \end{cases} \quad (48)$$

All translations represented by Eqs. (45)-(47) involve order $I \times J$ operations. Indeed, considering for example Eq. (45) or (47), for each $v = v_j, j = 0, \dots, J$, one must perform a one-dimensional cubic spline interpolation along x at all spatial points $\{x_i - v_j\Delta t/2\}, i = 0, \dots, I$, which in turn involves order I operations, both for computing the coefficients of the cubic spline representation (requires solving a tri-diagonal linear system of rank I) and for its evaluation at the interpolation points. The same total $I \times J$ scaling applies for the translation in the v direction defined by (46).

2. Sources to Poisson's Equation

For advancing the distribution from time t_{n-} to t_{n+} by carrying out the v advection (43), the force field $F(x, t_n)$ must first be computed. This involves the self-consistent electrostatic field $E_{\text{es}}^{\text{int}}(x, t_n)$, obtained by solving Poisson's equation (37), which in turn requires computing the electron density $n(x, t_n)$ at time t_n . When time stepping the system, $n(x, t_n)$ can at first only be calculated from $f(x, v, t_{n-})$, but, as a consequence of (43), this density would also be equivalent to the one derived from $f(x, v, t_{n+})$:

$$\begin{aligned} n(x, t_n) &= \int_{-\infty}^{+\infty} dv f(x, v, t_{n-}) \\ &= \int_{-\infty}^{+\infty} dv f(x, v - F(x, t_n)\Delta t, t_{n-}) \\ &= \int_{-\infty}^{+\infty} dv f(x, v, t_{n+}). \end{aligned}$$

One thus uses the following trapezoidal integration rule for estimating the density of each species at the spatial grid points:

$$n(x_i, t_n) \simeq \sum_{j=0}^J \Delta v_j f(x_i, v_j, t_{n-}), \quad (49)$$

with Δv_j the grid interval “centered” at v_j :

$$\Delta v_j = \begin{cases} (v_1 - v_0)/2, & \text{if } j = 0, \\ (v_{j+1} - v_{j-1})/2, & \text{if } j = 1, \dots, J-1, \\ (v_J - v_{J-1})/2, & \text{if } j = J. \end{cases} \quad (50)$$

3. Poisson Solver

Assuming an equidistant spatial grid $x_i = i\Delta x, i = 0, \dots, I$, with $\Delta x = L/I$, Eq. (37) for the electrostatic potential ϕ can be discretized with a centered, second order accurate finite difference scheme:

$$\frac{\phi_{i+1} + \phi_{i-1} - 2\phi_i}{\Delta x^2} = -\frac{1}{\epsilon_0} \sum_{\text{species}} q n_i, \quad (51)$$

where $\phi_i = \phi(x_i)$ and $n_i = n(x_i)$ is given by Eq. (49). Equation (51) defines a linear, tridiagonal system for the $\{\phi_i\}_{i=1, \dots, I}$, which must be completed with the periodic boundary conditions:

$$\phi_{i+I} = \phi_i.$$

The electrostatic field E_{es} is then computed from ϕ using again a centered, second order accurate finite differencing relation:

$$E_{\text{es},i}^{\text{int}} = -\frac{\phi_{i+1} - \phi_{i-1}}{2\Delta x}. \quad (52)$$

Making use of the periodic boundaries, the linear system (51) for $\{\phi_i\}$ can be reduced to an algebraic relation in Fourier space. To this end, one considers the discrete Fourier transform:

$$\phi_i = \sum_{k=0}^{I-1} \hat{\phi}_k \exp(\imath i k \frac{2\pi}{I}) \quad \Longleftrightarrow \quad \hat{\phi}_k = \frac{1}{I} \sum_{i=0}^{I-1} \phi_i \exp(-\imath i k \frac{2\pi}{I}),$$

where the notation $\imath = \sqrt{-1}$ has been chosen (in this sub-section only) to distinguish the imaginary unit from the index i used for the x -grid. In Fourier representation, the discretized

Poisson equation (51) becomes

$$\left[\frac{2}{\Delta x} \sin\left(\frac{k\pi}{I}\right) \right]^2 \hat{\phi}_k = \frac{1}{\epsilon_0} \sum_{\text{species}} q \hat{n}_k, \quad (53)$$

and in the same representation Eq.(52) reads

$$\hat{E}_{\text{es},k}^{\text{int}} = -\frac{\imath}{\Delta x} \sin\left(\frac{k2\pi}{I}\right) \hat{\phi}_k. \quad (54)$$

Combining Eqs. (53) and (54), one finds

$$\hat{E}_{\text{es},k} = -\frac{1}{\epsilon_0} \frac{(\imath/\Delta x) \sin(k2\pi/I)}{[(2/\Delta x) \sin(k\pi/I)]^2} \sum_{\text{species}} q \hat{n}_k.$$

The direct Fourier transform of the density, and the inverse transform required to obtain $E_{\text{es}}^{\text{int}}$ in real space, can be efficiently carried out with the fast Fourier transform (FFT) algorithm, which requires operations of order $I \log(I)$.

C. Extracting the Frequency Shift using a Hilbert Transform Method

An accurate diagnostic for computing the frequencies of the waves is essential to obtain good estimates of the small non-linear shifts. This was achieved by using a standard signal processing procedure based on the Hilbert transform, which permits the extraction of the time varying amplitude and frequency of an oscillating signal.

Let us assume that $u(t)$ is the time varying oscillating signal, *i.e.* a real function of time. For our problem of interest, this would typically be the fluctuating electrostatic potential field associated to the wave at a given spatial reference point $x = x_0$: $u(t) = \phi(x_0, t)$. The goal is to extract the envelope $a(t)$ and the phase $\theta(t)$ of the signal $u(t) = a(t) \cos[\theta(t)]$. To this end, one defines the analytic representation $u_a(t)$ of $u(t)$ as follows:

$$u_a(t) = \lim_{\epsilon \rightarrow 0} \frac{i}{\pi} \int dt' \frac{u(t')}{(t - t') + i\epsilon}.$$

Using the relation

$$\lim_{\epsilon \rightarrow 0} \frac{1}{(t - t') + i\epsilon} = \frac{P}{t - t'} - i\pi \delta(t - t'),$$

which is to be interpreted in terms of distributions, P and δ standing respectively for the principal value and the Dirac function, one obtains:

$$u_a(t) = u(t) + \frac{i}{\pi} P \int dt' \frac{u(t')}{t - t'} = u(t) + i \tilde{u}(t), \quad (55)$$

with

$$\tilde{u}(t) = \frac{1}{\pi} P \int dt' \frac{u(t')}{t - t'} \quad (56)$$

the so-called Hilbert transform of $u(t)$. In the particular case of a periodic function $u(t)$ with period τ , making use of the partial fraction expansion

$$\pi \cot(\pi z) = \lim_{N \rightarrow +\infty} \sum_{n=-N}^{+N} \frac{1}{z + n},$$

the Hilbert transform (56) becomes:

$$\tilde{u}(t) = \frac{1}{\tau} P \int_0^\tau dt' u(t') \cot \left[\frac{\pi(t - t')}{\tau} \right].$$

The modulus and argument of the analytic function $u_a(t) = a(t) \exp[i\theta(t)]$ provides the desired envelope and phase of $u(t)$:

$$a(t) = |u_a(t)|, \quad (57)$$

$$\theta(t) = \arg[u_a(t)]. \quad (58)$$

According to (55), one indeed has $u(t) = \text{Re}[u_a(t)] = a(t) \cos[\theta(t)]$. In Eq. (58), the \arg function is not restricted to the principal value in $[-\pi, \pi]$. Instead, this multi-valued function is evaluated such as to ensure continuity over the $\pi + n2\pi$ borders. The instantaneous frequency is then obtained from

$$\Omega(t) = \frac{d}{dt} \theta(t).$$

An intuitive understanding of and practical approach for computing the analytic representation $u_a(t)$ is obtained by transforming this function to Fourier space. If $\hat{u}(\omega)$ is the Fourier transform of $u(t)$:

$$u(t) = \int d\omega \hat{u}(\omega) \exp(i\omega t) \quad \longleftrightarrow \quad \hat{u}(\omega) = \frac{1}{2\pi} \int dt u(t) \exp(-i\omega t) \quad (59)$$

one can show, starting from Eq. (56), that the Fourier transform $\hat{\tilde{u}}(\omega)$ of the Hilbert transform $\tilde{u}(t)$ of $u(t)$ is given by

$$\hat{\tilde{u}}(\omega) = -i \text{sgn}(\omega) \hat{u}(\omega), \quad (60)$$

where sgn is the signum function. The Hilbert transform on a function thus has the effect of shifting the Fourier components by $\pm\pi/2$, and in particular transforms a \cos into a \sin

function and a sin function into $-\cos$. One therefore clearly understands from (55) how u_a gives a complex phaser representation of $u(t)$, providing the desired envelope and phase according to Eqs. (57)-(58).

From Eqs. (55) and (60), the Fourier transform $\hat{u}_a(\omega)$ of $u_a(t)$ is given by

$$\hat{u}_a(\omega) = \hat{u}(\omega) + \hat{\tilde{u}}(\omega) = [1 + \text{sgn}(\omega)]\hat{u}(\omega) = 2H(\omega)\hat{u}(\omega), \quad (61)$$

where H is again the Heaviside function. This last relation determines in principal a practical approach for computing the analytic representation $u_a(t)$: Take the Fourier transform of $u(t)$, remove the negative frequency spectrum according to (61), and finally apply the inverse Fourier transform to obtain $u_a(t)$. This procedure is indeed appropriate for a function $u(t)$ having a finite support or in the case of a periodic function. In the latter case, instead of the Fourier transform (59), one would consider the Fourier series of $u(t)$ with coefficients \hat{u}_m :

$$u(t) = \sum_{m=-\infty}^{+\infty} \hat{u}_m \exp[i m(2\pi/\tau) t] \quad \longleftrightarrow \quad \hat{u}_m = \frac{1}{\tau} \int_0^\tau dt u(t) \exp[-i m(2\pi/\tau) t]$$

and relations (60) and (61) become

$$\hat{\tilde{u}}_m = -i \text{sgn} \hat{u}_m, \quad \text{and} \quad \hat{u}_{a,m} = 2H(m)\hat{u}_m, \quad (62)$$

where the signum and Heaviside function of the integer argument m are defined as $\text{sgn}(m) = -1, 0, 1$, for $m < 0$, $m = 0$, $m > 0$, respectively, and $H(m) = [1 + \text{sgn}(m)]/2$.

In practice, the signal $u(t)$ obtained from the simulation is only known at a sampling set of N equidistant time steps t_n : $u_n = u(t_n)$, $n = 0, \dots, N-1$. In this case, the Fourier series is replaced by the discrete Fourier transform (DFT), given by

$$u_n = \sum_{m=0}^{N-1} \hat{u}_m \exp(i nm2\pi/N) \quad \longleftrightarrow \quad \hat{u}_m = \frac{1}{N} \sum_{n=0}^{N-1} u_n \exp(-i nm2\pi/N),$$

which provides the N Fourier coefficients \hat{u}_m , $m = 0, \dots, N-1$. The now *discretized* Hilbert transform (DHT) \tilde{u}_n and analytic representation $u_{a,n}$ of the data sampling u_n are defined so that the relations (62) between the corresponding discretized Fourier coefficients \hat{u}_m , $\hat{\tilde{u}}_m$, and $\hat{u}_{a,m}$ still hold. The signum and Heaviside functions need however to be appropriately

defined to account for the N -periodicity:

$$\begin{aligned} \text{for } N \text{ even: } \quad \text{sgn}(m) &= \begin{cases} 0, & m = 0, N/2 \\ 1, & m = 1, \dots, N/2 - 1 \\ -1, & m = N/2 + 1, \dots, N-1 \end{cases}, \\ \text{for } N \text{ odd: } \quad \text{sgn}(m) &= \begin{cases} 0, & m = 0 \\ 1, & m = 1, \dots, (N-1)/2 \\ -1, & m = (N-1)/2 + 1, \dots, N-1 \end{cases}, \end{aligned}$$

the Heaviside function being still given by $H(m) = [1 + \text{sgn}(m)]/2$. One can show that in real space the DHT then corresponds to a convolution relation of the form

$$\tilde{u}_n = \sum_{n'=0}^{N-1} h_{n-n'} u_{n'},$$

where this last relation makes use of the N -periodicity of the samples, with the kernel h_n of the transform such that $h_0 = 0$ and for $n = 1, \dots, N-1$:

$$h_n = \begin{cases} \frac{1-(-1)^n}{N} \cot(\pi n/N), & \text{for } N \text{ even,} \\ \frac{1}{N} \frac{\cos(\pi n/N) - (-1)^n}{\sin(\pi n/N)}, & \text{for } N \text{ odd.} \end{cases}$$

Furthermore, the sampled signal is usually not exactly periodic. This issue is addressed as follows: The time sampling interval $[t_0, t_N]$ is chosen such that the boundaries t_0 and t_N correspond to two local maxima of the oscillating signal u_n . Within this interval, all other local maxima are identified. Using an interpolation scheme (e.g. cubic spline) through these maxima, a first estimate of the signal's envelope A_n at the sampling points t_n , $n = 0, \dots, N-1$ is obtained. One then considers the normalized sample $U_n = u_n/A_n$, which by construction is now periodic. Taking its discretized Fourier transform, applying relation (62) and performing the inverse Fourier transform, one can conveniently obtain the complex sampling $U_{a,n}$ of the corresponding analytic representation. By denormalizing, one finally obtains the analytic representation $u_{a,n} = A_n U_{a,n}$ of the original signal u_n . The sampled envelope a_n and phase θ_n are then simply obtained according to relations (57) and (58):

$$a_n = |u_{a,n}|, \tag{63}$$

$$\theta_n = \arg(u_{a,n}). \tag{64}$$

In practice, an estimate of the average frequency over a time interval $[t_1, t_2]$ is obtained by taking the slope of a linear regression fit through the data points (t_n, θ_n) falling within this time interval.

Illustrations of this phase and envelope extraction based on the Hilbert transform are shown in Figs. 5 and 8. Figure 5 presents the amplitude evolution, obtained using relation (63), of a standing EPW with finite initial value from which the damping rate is extracted, both in the initial and later evolution phase, using an exponential fit. A linear fit to the phase evolution (not shown), obtained using relation (64) provides the real frequencies as well. This frequency extraction is however clearly illustrated in the case of a driven IAW in Fig. 8. A measure of error in the frequency obtained is provided by computing the result when different time intervals are chosen. In the example in Fig. 8, the frequency shifts obtained with five different time intervals varying from 1 to $4 \cdot 10^4 \omega_{pe}^{-1}$ differed by less than 3% from the average. A similar result was found for $ZT_e/T_i = 30$ for a similar wave amplitude. For the smallest wave amplitudes shown in Fig. 11, the estimated error in the frequency shift was up to 8%.

IV. VLASOV SIMULATION RESULTS

In this section, for both EPWs (Sec. IV A) and IAWs (Sec. IV B), the frequencies of the non-linear BGK-like waves obtained by the Vlasov simulations are compared to the theoretical estimates presented in Sec. II. The frequencies of the finite amplitude, steady state waves are computed with the methods described in Sec. III C. A more detailed analysis is presented subsequently by comparing the fraction of trapped ions and electrons in an IAW to theory (Sec. IV C) for both adiabatic or sudden wave generation. As will be shown in Sec. IV C, for lower wave amplitudes such that the trapping width $\Delta v_{tr}/v_{th} = 2(|q|\phi_0/T)^{1/2}$ for a given species is small, the corresponding fraction of trapped particles is essentially the same for sudden and adiabatic generation and thus does not discriminate between these two scenarios. Only for larger relative trapping widths does this trapped fraction depend on the type of wave generation. In Sec. IV D, an even more detailed analysis of the particle dynamics is therefore carried out by studying the actual particle distributions from the simulations and comparing them to the theoretical predictions. Examples of electron and ion distributions for IAWs illustrate in detail the energy dependence of the trapped and

resonant passing particles from the simulations in steady state along with the theoretical distributions for sudden and adiabatic generation. These examples of energy distributions in particular show that the electrons in a driven IAW are very well represented by an adiabatic distribution.

In Sec. IV B, by considering three values of the effective ratio ZT_e/T_i , the non-linear frequency shift of IAWs are estimated for different wave amplitudes and compared to theory. For lower amplitudes, $e\phi_0/T_e \lesssim 0.03$, the agreement with the theory for frequency shifts resulting from particle trapping is quite good. For larger amplitudes, $e\phi_0/T_e \gtrsim 0.03$, the shifts are systematically more positive. This coincides with the development of significant harmonic content in the wave. As a result, the fraction of trapped ions and electrons also diverges at these higher amplitudes from the theoretical predictions which assume a sinusoidal wave. However, when the actual waveform of the electrostatic potential from the simulation is used, the theoretical value for trapped fraction, adiabatic or sudden as appropriate, is altered and agrees very well with the simulation results. In the examples of distribution functions, the effect of non-sinusoidal waveforms on the energy dependence of trapped and resonant passing particles supports in detail the frequency shift analysis. The fluid-like non-linear frequency shift from ion acoustic wave harmonics ($\propto |\phi|^2$) is positive and of the correct magnitude to explain the difference between the simulation results and the kinetic theory, neglecting harmonics.

A. Non-Linear Frequency Shifts of EPWs

In Fig. 4, the non-linear frequency shift of an electron plasma wave with $k\lambda_{De} = 1/3$ is displayed as a function of the field amplitude, $e\phi_0/T_e$. Three estimates are in fact shown: 1) The approximate analytic solution given by Eq. (19), with the phase velocity computed using the Bohm-Gross dispersion relation (17), 2) the numerical solution to Eq. (6), *i.e.* computing the complex root of the complex non-linear dispersion, $\epsilon_{NL}(k, \omega_{NL}; \phi_0) = 0$, and 3) numerically computing the real root of the real non-linear dispersion, $\Re[\epsilon_{NL}(k, \omega_{NL,r}; \phi_0)] = 0$. Note that even in the limit $e\phi_0/T_e \rightarrow 0$ the real frequencies obtained from these three procedures differ especially as $k\lambda_{De}$ increases.

For $k\lambda_{De} = 1/3$ considered here, the zero-amplitude, numerically-obtained real part of the complex root provides $\Re(\omega_L) = 1.200\omega_{pe}$, while the real solution considering only the

real part of the dispersion relation gives a slightly smaller value $\omega_{L,r} = 1.194\omega_{pe}$. The Bohm-Gross frequency, $\omega_{BG} = 1.155\omega_{pe}$, obtained from Eq. (17) provides the smallest value. For larger $k\lambda_{De}$, the difference between these roots further increases. In Fig. 4, the difference between the frequency for finite amplitude and the corresponding frequency for zero amplitude (the actual frequency shift) is therefore plotted for all three considered estimates, so that all curves start at the origin. Compared to either numerical solution, the approximate analytic solution overestimates the frequency shift. The origin for these differences can be traced back to the exponential term in Eq. (19), whose value is very sensitive to the magnitude of ω/kv_{the} . The larger the linear frequency, the smaller this term becomes.

In light of the previous discussion, it is thus not obvious with respect to which reference value the frequency shifts from the simulation results are to be computed. One can argue that these shifts should be estimated with respect to the real frequency for which the *real part* of the non-linear dispersion is zero ($\Re[\epsilon_{NL}(k, \omega_{NL,r}; \phi_0)] = 0$), as the waves studied in the simulations have essentially constant amplitude (quasi BGK-like), albeit with some noticeable modulation on the scale of the trapping frequency. However, in the initial state for which the electron distribution is a Maxwell-Boltzmann in velocity, the wave is damped and responds resonantly at the frequency corresponding to the linear solution of the *complex* dispersion relation. Lindberg *et al.* [12] address this issue directly and argue that, in the limit of vanishing amplitude, the Vlasov dispersion relation [59] with no damping is the natural choice. In fact, none of these frequencies proved to be appropriate in all cases. It was found that the best procedure is to first identify a fit of the form $\omega_{NL}^{fit}(\phi_0) = \omega_{NL}^{fit}(0) + C\phi_0^{1/2}$ to the frequencies $\omega_{NL}^{sim}(\phi_0)$ of the non-linear modes from the simulations obtained for different finite amplitudes ϕ_0 , where $\omega_{NL}^{fit}(0)$ and C are fitting coefficients determined through a least mean square approach. Note the fit was determined by using only the low-amplitude portion of simulation's nonlinear frequencies which scale well with $\phi_0^{1/2}$. The frequency shift for the simulation results at any finite amplitude ϕ_0 is then determined as $\delta\omega_{NL}^{sim}(\phi_0) = \omega_{NL}^{sim}(\phi_0) - \omega_{NL}^{fit}(0)$. Let us point out that this approach for determining the frequency shift for the simulation results was applied to IAWs as well.

As discussed in Sec III A, the EPW is either initialized as a sinusoidal spatial modulation of the density or is driven by an external, sinusoidal traveling-wave ponderomotive potential. In the former case, the system responds by launching two waves with same amplitude

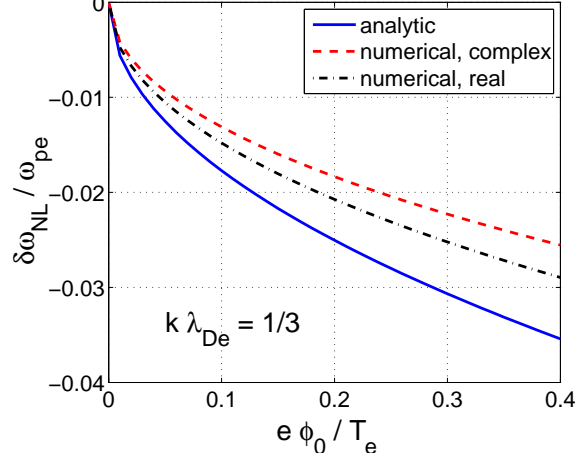


FIG. 4: (color online) Three estimates of the non-linear frequency shifts of an EPW with $k\lambda_D = 1/3$: 1) the approximate analytic solution given by Eq. (19), 2) shift based on the real part of the numerically computed root of the complex non-linear dispersion $\epsilon_{NL}(k, \omega_{NL}; \phi_0) = 0$, and 3) shift based on the numerically computed real root of the real non-linear dispersion $\Re[\epsilon_{NL}(k, \omega_{NL,r}; \phi_0)] = 0$.

traveling in opposite directions, resulting in a standing wave. The non-linear resonant electron regions for the forward and backward propagating waves, of width $\sim \Delta v_{tr,e}$ around the phase velocities $\pm v_\phi$, are well separated in velocity as $|v_\phi| > v_{th,e} > \Delta v_{tr,e}$, and these two waves can thus be assumed to evolve independently of each other, *i. e.* the superposition principle applies as for the linear case. Initially, the waves decay in time at the Landau damping rate as shown in Fig. 5. Two examples are shown: one of a moderately damped EPW with $k\lambda_{De} = 0.3$ and the other a strongly damped EPW with $k\lambda_{De} = 0.425$. The measured frequency and damping rate at early times when the wave is decaying in amplitude, $\omega/\omega_{pe} = 1.164 - 0.01580i$, resp. $\omega/\omega_{pe} = 1.304 - 0.08835i$, is nearly equal to the frequency and damping rate found from the (least damped) solution to the complex dispersion relation for $\phi_0 = 0$, *i.e.* $\omega_L/\omega_{pe} = 1.160 - 0.01262i$, resp. $\omega_L/\omega_{pe} = 1.318 - 0.08526i$. Other eigenmodes at different frequencies will be launched by this initial perturbation as well, but will damp away more quickly, *i.e.* within a short initial transient time interval, so that only the damping rate of the least damped oscillation is effectively measured with this technique.

If the initial amplitude is large enough, some of the resonant electrons become trapped and, after half a bounce time, give their energy back to the wave, whose amplitude increases again as a result. Still half a bounce time later, the oscillation motion of trapped particles in

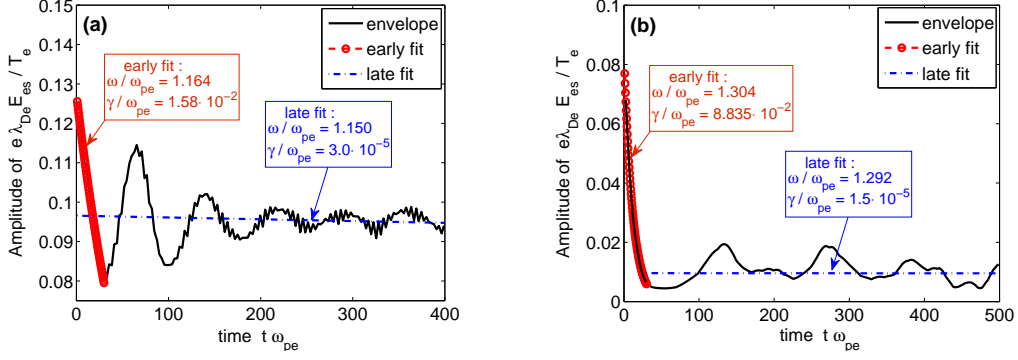


FIG. 5: (color online) Time evolution of the electrostatic field amplitude E_{es} for a standing EPW when the charge density is initialized to an amplitude and wavenumber of (a) $(\delta N/N = 5.0 \cdot 10^{-2}, k\lambda_D = 0.3)$, and (b) $(\delta N/N = 5.0 \cdot 10^{-2}, k\lambda_D = 0.425)$ respectively. In both cases, a fit to the early time behavior provides a damping rate and frequency in close agreement with the solution to the complex linear dispersion relation. A fit to the time history after the initial decay provides however a reduced frequency as well as an essentially undamped wave.

the electrostatic potential well of the wave is completed, and the wave again loses energy to these particles, so that its amplitude again decreases. This results in a periodic modulation of the wave amplitude at an effective bounce frequency. The amplitude of this modulation however decreases over time as a result of filamentation of the distribution of particles in the trapping region, itself due to different bounce periods between deeply and barely trapped particles [41]. After a certain number of bounce times, a quasi-steady, BGK-like state is thus established. According to the theory summarized in Sec. II, this non-linear wave acquires a frequency shift, which, for the initial value cases considered here, may be estimated assuming the 'sudden' limit for the wave generation. This non-linear trapping phenomena is clearly illustrated by the case $k\lambda_{De} = 0.3$ shown in Fig. 5, for which the amplitude oscillations at the bounce frequency are nearly periodic. In the $k\lambda_{De} = 0.425$ case, the non-linear oscillations are clearly visible as well, but are however less regular. This results from the fact that for larger values of $k\lambda_{De}$, the phase velocity v_ϕ is lower and for same amplitude of the wave the trapping region digs deeper into the bulk of the distribution, resulting in a larger fraction of trapped particles, and thus in a potentially more irregular non-linear evolution.

In the driven case, the external field $E_{\text{es}}^{\text{ext}}(x, t)$, defined in Eq. (38), is given a frequency and wavelength that satisfy the linear complex dispersion relation for EPWs. If the time

interval t_{drive} over which the external drive is maintained is such that $t_{\text{drive}} \gg 1/\omega_{be} \gg 1/\omega_{pe}$, a non-linear wave with essentially steady amplitude is obtained. Varying t_{drive} , propagating waves with different amplitudes ϕ_0 may be generated in this way. Furthermore, if the EPW is driven sufficiently slowly so that $|\partial \ln \phi_0 / \partial t| \ll \omega_{be}$, where ϕ_0 is the self-consistent wave potential amplitude and $\omega_{be} \sim \phi_0^{1/2}$ is the instantaneous bounce frequency of the resonant electrons, one expects to verify the conditions for an adiabatic generation of the wave. Note that at the beginning of such a driven simulation, there is inevitably a (short) time interval during which $\phi_0 \sim 0$ and the above inequality cannot be satisfied.

1. EPW. Intermediate wavenumber $k\lambda_{De} = 1/3$

The dependence of the frequency shift of EPWs on wave amplitude was systematically studied by carrying out a series of simulations in which either an initial sinusoidal density perturbation or an external propagating driver potential were chosen to generate a self-consistent standing, respectively propagating, wave. Here one considers in detail the non-linear evolution of EPWs for $k\lambda_{De} = 1/3$, for which the linear, complex dispersion relation, $\epsilon_L(\omega_L) = 0$, provides the solution $\omega_L/\omega_{pe} = 1.200 - 2.587 \cdot 10^{-2}i$, $\Re[\partial \epsilon_L(\omega_L)/\partial \omega] = 2.472/\omega_{pe}$ and the phase velocity $v_\phi = 3.6 v_{th,e}$. The real frequency that satisfies $\Re[\epsilon_L(\omega_{L,r})] = 0$, *i.e.* $\omega_{L,r}/\omega_{pe} = 1.194$, as well as $\partial \Re[\epsilon_L(\omega_{L,r})]/\partial \omega_r$ are nearly the same as the values from the complex root. The Bohm-Gross frequency, used in the analytic estimate for the frequency shift [see Eq. (19)], is however smaller, *i.e.* $\omega_{BG} = 1.154\omega_{pe}$ and the approximation $\partial \epsilon_{BG}(\omega_{BG})/\partial \omega \simeq 2/\omega_{pe}$ is considered in this case. As described above, a fit of the form $\omega_{NL}^{fit}(\phi_0) = \omega_{NL}^{fit}(0) + C \phi_0^{1/2}$ to the data for the non-linear frequency as a function of the square root of the amplitude ϕ_0 was taken for both the initial value and the driven runs. Extrapolating these fits to $\phi_0 = 0$, one finds the frequency $\omega_{NL}^{fit}(0)$, which for both cases provided $1.198\omega_{pe}$. The frequency shifts for the simulation results, estimated by $\delta\omega_{NL}^{sim} = \omega_{NL}^{sim} - \omega_{NL}^{fit}(0)$, as a function of the self-consistent wave amplitude are plotted in Fig. 6. The sudden and adiabatic theory curves for the non-linear frequency shift $\delta\omega_{NL}$ are also shown for comparison. For these theoretical curves, the phase velocity used in evaluating the analytic formula (19) is estimated with $\omega_{L,r}$, not the Bohm-Gross frequency ω_{BG} . In addition, the correct value of $\partial \Re[\epsilon_L(\omega_{L,r})]/\partial \omega_r$, not $2/\omega_{pe}$, is used in this derivation of $\delta\omega_{NL}$. The frequency shifts from the analytic theory for the adiabatic (resp. sudden)

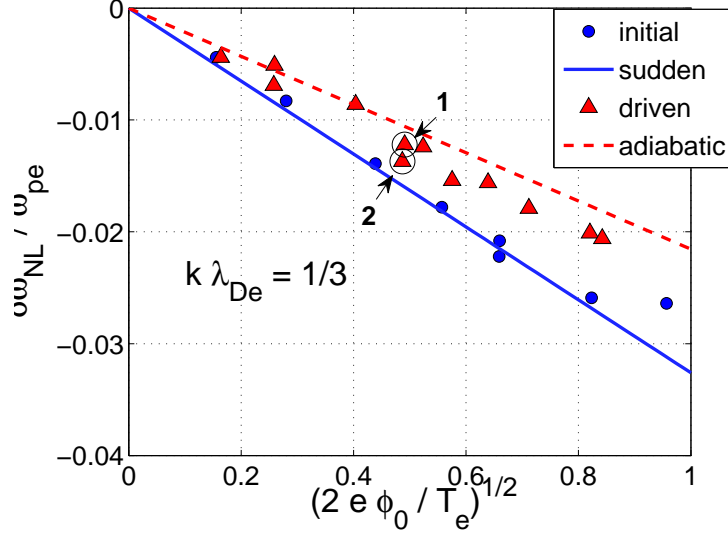


FIG. 6: (color online) EPW case with $k\lambda_{De} = 1/3$. Frequency shifts as a function of $\sqrt{2e\phi_0/T_e}$ measured from simulations. Both initial value (blue circles) and driven waves (red triangles) results are shown and compared to theoretical estimates given by Eq. (19) in the sudden (blue full line) and adiabatic (red dashed line) wave generation limit.

approximation match quite well the shifts from the simulations of the waves driven by an external potential (resp. initialized at finite amplitude). The frequency shifts for the initialized wave simulations are thus systematically larger (in absolute value) than for the driven wave simulations. In the driven case, the frequency shifts measured once a steady state wave amplitude is achieved can nonetheless depend significantly on the drive history, which is not ideally adiabatic in the simulations. In Fig. 6 for example, there are two shifts obtained from two different simulations plotted for $\sqrt{2e\phi_0/T_e} \sim 0.5$, corresponding to the triangular data points labeled '1' and '2'. The wave corresponding to the data point '2' with the larger shift was initially driven to a larger amplitude than the wave relative to the data point '1', but then finally relaxed to a similar amplitude. We found that the distributions achieved in these simulations in fact lie between the sudden and adiabatic predictions in some cases, and, thus, neither the sudden coefficient α_s nor the adiabatic coefficient α_{ad} in Eq. (19) is appropriate.

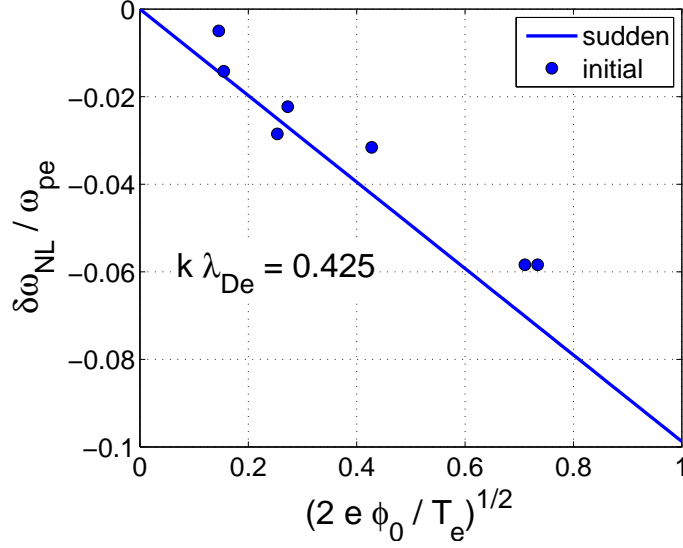


FIG. 7: (color online) Initial value EPW case with $k\lambda_{De} = 0.425$. Frequency shifts as a function of $\sqrt{\phi_0}$ measured from simulations (blue circles). Comparison with theoretical estimate (blue full line) given by Eq. (19) in the sudden wave generation limit.

2. EPW. Larger wavenumber $k\lambda_{De} = 0.425$

Here one considers the non-linear state of EPWs for the larger wavenumber $k\lambda_{De} = 0.425$, for which the linear, complex dispersion relation has the solution $\omega_L/\omega_{pe} = 1.318 - 0.08526i$, giving a phase velocity $v_{ph} = 3.1 v_{th,e}$. The solution to the real dispersion relation however provides $\omega_{L,r}/\omega_{pe} = 1.272$ and the Bohm-Gross frequency is given by $\omega_{BG}/\omega_{pe} = 1.242$. The derivative of the complex dielectric function is $\Re[\partial\epsilon_L(\omega_L)/\partial\omega] = 2.354/\omega_{pe}$. From the fit to the simulation data for the non-linear frequencies as a function of the wave amplitude extrapolated to $\phi_0 = 0$, one finds $\omega_{NL}^{fit}(0) = 1.312$, a value intermediate between the two numerical solutions $\Re(\omega_L)$ and $\omega_{L,r}$. In this case, with lower phase velocity compared to $k\lambda_{De} = 1/3$, a much larger number of electrons will be trapped by a wave of a given amplitude than in the case with $k\lambda_D = 1/3$ and the corresponding frequency shifts are thus larger as well. Here, only initialized waves were considered in the simulations and the corresponding frequency shifts, $\delta\omega_{NL}^{sim} = \omega_{NL}^{sim} - \omega_{NL}^{fit}(0)$, shown in Fig. 7, follow the sudden theory limit.

B. Non-Linear Frequency Shifts of IAWs

Initializing a finite amplitude standing ion acoustic wave with kinetic electron dynamics proves to be an impractical technique for launching independently propagating traveling waves as the electron trapping regions for the left and right traveling waves overlap. Thus, the superposition principal invoked for interpreting the standing EPWs is not valid. This results from the fact that the widths $\Delta v_{\text{tr},e}$ of the electron trapping regions are in general much larger than the wave phase velocity v_ϕ , except for very small wave amplitudes. For an IAW one indeed has

$$\frac{\Delta v_{\text{tr},e}}{v_\phi} \simeq 2 \sqrt{\frac{e\phi_0}{T_e}} \sqrt{\frac{m_i}{Z m_e}} \sim 1 \quad \Longleftrightarrow \quad \frac{e\phi_0}{T_e} \sim \frac{1}{4} \frac{Z m_e}{m_i} \sim 10^{-3},$$

having approximated v_ϕ with the cold-ion sound speed c_s . As with EPWs, it is however practical to generate finite-amplitude traveling IAWs with an external driver. Note that the ratio of the electron bounce frequency $\omega_{b,e}$ to the IAW frequency $\omega_a \simeq k c_s$ is of the same order as the ratio $\Delta v_{\text{tr},e}/v_\phi$ ($\omega_{b,e}/\omega_a \simeq \Delta v_{\text{tr},e}/2 v_\phi$) and thus quickly becomes very large as the wave grows to finite amplitude. If the amplitude of the IAW evolves on time scales of the order or smaller than ω_{IAW} , one expects the electrons to respond essentially adiabatically.

Let us also recall here that the effective parameters characterizing the kinetic dynamics of an IAW, assuming a single ion species, are the normalized wavenumber $k\lambda_{De}$, the electron/ion temperature ratio ZT_e/T_i , and mass ratio Zm_e/m_i , where Z is the ionization degree of the ions. A normalized amplitude, e.g. $e\phi_0/T_e$, is naturally also essential for characterizing non-linear, finite amplitude waves. In this section, simulation results of propagating IAWs are presented. These waves are driven with an external field as given in Eq. (38), with the frequency ω^{ext} usually chosen as the real part of the complex frequency that satisfies the complex linear dispersion relation $\epsilon_L = 0$, ϵ_L being given by Eq. (5) and with the sum extending over both electron and ion species. The external field is applied only to the electrons, thus emulating the ponderomotive drive in SBS, and is ramped up to its full value over a time $t_{\text{ramp}} \sim 5 - 7 \omega_a^{-1}$, *i.e.* about one wave period, and then kept on for a number of wave periods (typically 10 – 30) after which it is turned off. The electron bounce frequency quickly becomes greater than the growth rate of the driven wave (which is typically of the order of or smaller than ω_a), so that the condition for adiabatic response is satisfied for the electrons except for the earliest times in the evolution when the wave amplitude is very small. Even after the external driver is turned off, the wave amplitude may

exhibit slow oscillations on the ion bounce frequency time scale as the wave and resonant ion particles exchange energy. These oscillations, which ultimately damp out as the wave reaches its BGK-like state, reflect a non-adiabatic evolution of the ion distribution.

As described in Sec. II B, the relative importance between the positive electron and negative ion contributions to the frequency shift of an IAW is mainly determined by the parameter $Z T_e/T_i$. Three cases have therefore been considered: $Z T_e/T_i = 30$, $Z T_e/T_i = 10$, and $Z T_e/T_i = 6$, all with $k \lambda_{De} = 0.3$. The electron frequency shift is expected to be much larger than the negative ion frequency shift in the first case, while the shifts should be similar and nearly cancel in the second case, finally, the negative ion shift should be largest in the third case.

1. IAW case $Z T_e/T_i = 30$

In this case, one considers a fully ionized Helium plasma ($Z = 2$, $m_i/m_e = 4 \times 1836$, so that $Z/A = 1/2$, A the atomic mass number) with a temperature ratio $T_e/T_i = 15$, in which an IAW with wavenumber $k \lambda_{De} = 0.3$ is driven at its linear resonant frequency $\Re(\omega_L)$, where $\omega_L/\omega_{pe} = 5.015 \cdot 10^{-3} - 4.264 \cdot 10^{-5}i$ is computed numerically from the complex linear dispersion relation. An example of a corresponding simulation is shown in Fig. 8, where the external drive is turned on for a time $t_{\text{drive}} = 1.5 \cdot 10^4 \omega_{pe}^{-1} \simeq 75 \omega_a^{-1}$ at an amplitude $E_0^{\text{ext}} = 5 \times 10^{-4} T_e/(e \lambda_{De})$. The internal wave amplitude reaches its peak $E_0^{\text{int}} = 1.5 \times 10^{-2} T_e/(e \lambda_{De})$ shortly before the drive is turned off, as can be seen in Fig. 8. The average amplitude and frequency are measured over the time interval $3.0 \cdot 10^4 < \omega_{pe} t < 4.9 \cdot 10^4$. The slow oscillations in the amplitude after the drive is off can be traced to the small fraction of trapped ions, with deeply trapped bounce frequency $\omega_{b,i} \simeq 1.1 \cdot 10^{-3} \omega_{pe}$, *i.e.* about one fifth of the frequency of the IAW. The electron bounce frequency $\omega_{b,e}$ is $\sqrt{m_i/(Z m_e)} \simeq 60$ times larger than the ion bounce frequency, so that the growth rate of the wave amplitude is clearly slower than $\omega_{b,e}$. The adiabatic assumption for electrons should thus be satisfied. In this example, about 15% of the electrons are trapped in the final wave and the electron velocity distribution is flattened in a trapping region of width $2 \Delta v_{\text{tr},e}/v_{\text{th},e} \simeq 0.86$ centered at $v_\phi/v_{\text{th},e} = 1.7 \cdot 10^{-2} \simeq 0$, as shown in Fig.9 at time $t = 5 \cdot 10^4 \omega_{pe}^{-1}$ and spatial location $x/\lambda_{De} = 10.5$, *i.e.* a point near the peak of the wave's electrostatic potential $\phi(x, t)$ (corresponding to a minimum of the potential well $-e\phi(x, t)$ seen by the electrons) at the end of the simulation.

In Fig. 10, the normalized frequency shifts $\delta\omega_{\text{NL}}/(k c_s)$ of IAWs obtained from a number of Vlasov simulations are plotted as a function of $\sqrt{2e\phi_0/T_e}$. The simulated IAWs were driven at the frequency $\Re(\omega_L)$ with varying driver amplitudes E_0^{ext} and time durations t_{drive} to obtain different amplitudes ϕ_0 . Exceptions are the largest amplitude cases which were driven at a slightly upshifted frequency, thus helping to avoid the de-phasing between the driver and the wave resulting from the non-linear frequency shift (positive in this case). According to theory, see Eq. (24), the shift should be a linear function of $\sqrt{\delta N/N} = \sqrt{e\phi/T_e}$. At lower amplitudes, *i.e.* $\sqrt{2e\phi_0/T_e} \lesssim 0.25$, the simulations agree very well with the theoretical predictions assuming an adiabatic wave generation for electrons. The ion contribution predicted by theory (whether sudden or adiabatic) is insignificant in this case and the effective shift is thus dominated by the positive electron contribution. The phase velocity used in Eq. (24) is evaluated from the complex linear frequency ω_L . This phase velocity is slightly bigger than the analytic approximation given by Eq. (25). In this case of large $Z T_e/T_i$, the estimate for $\delta\omega_{\text{NL}}$ is however unaffected as the ion contribution to the shift is negligible. For smaller values of $Z T_e/T_i$, this difference is significant as the next sections will show. The theory curves are however corrected by the fact that the derivative of the dielectric function, $\Re[\partial\epsilon_L(\omega_L)/\partial\omega]$, is about 10% larger than the analytical estimate (23) used to obtain Eq. (24).

Simulations with Hydrogen ions ($Z = 1$, $m_i/m_e = 1836$, $Z/A = 1$), still with the same temperature ratio $Z T_e/T_i = 30$ and the same wavenumber $k\lambda_{De} = 0.3$, were carried out as well. In this case, the linear frequency $\omega_a/\omega_{pe} \simeq k\lambda_{De} c_s/v_{\text{th},e} \sim \sqrt{Z m_e/m_i}$ is $\sqrt{2}$ larger than for Helium, but the ratio $v_\phi/v_{\text{th},i} \simeq \sqrt{Z T_e/T_i}$ remains basically the same ($v_\phi/v_{\text{th},i} = 5.548$ in both cases) and, as expected from Eq. (24), the simulation results yield very similar values for the normalized frequency shift $\delta\omega_{\text{NL}}/(k c_s)$, as shown in Fig. 10. In normalized units, the effective mass ratio $Z m_e/m_i$ thus does not significantly affect the non-linear kinetic dynamics of the wave, as long as $Z m_e/m_i \ll 1$.

We note from Fig. 10 that the frequency shifts obtained from the simulations for amplitudes $\sqrt{2e\phi_0/T_e} \gtrsim 0.25$ are larger than predicted by the theoretical estimate. Although some ion trapping starts to occur at larger amplitude leading to its time modulation pointed out in Fig. 8, the cause for this deviation is not to be found in the ion dynamics, whose negative contribution to the shifts tends to decrease, not increase, the total positive frequency shifts. The subsequent sections will show that the fraction of trapped electrons also

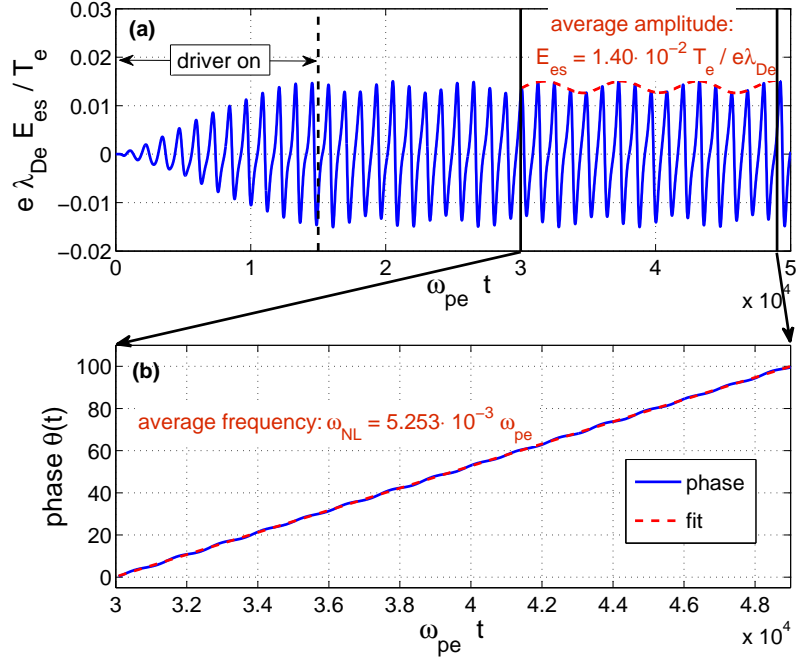


FIG. 8: (color online) Driven IAW case $Z T_e/T_i = 30$. a) Internal electric field E_{es}^{int} and b) phase $\theta(t)$ of the wave as a function of time t . The frequency and average amplitude are measured over the interval $3.0 \cdot 10^4 < \omega_{pe} t < 4.9 \cdot 10^4$. The slope of the linear fit to the phase allows the frequency to be extracted. The driver electric field is $E_0^{\text{ext}} = 5 \times 10^{-4} T_e / (e \lambda_{De})$

deviates from the theory at these larger wave amplitudes. Examination of the wave's spatial dependence shows that the wave is noticeably steepened, *i.e.* there is significant second harmonic content for waves with such large amplitudes. In Sec. II B 2, a derivation of a frequency shift, proportional to ϕ_0^2 , from wave harmonics was obtained from the cold ion fluid equations. Adding this shift [see Eq. (33)] to the trapped particle frequency shift results in better agreement (dashed red curve in Fig. 10). As shown in Fig. 14, this calculation underestimates however the amplitude of the 2nd harmonic. Using the fit $\phi_2 = 1.5\phi_0^{1.58}$ to the simulation values in Eq. (32) for the relation between ϕ_0 and ϕ_2 instead of Eq. (31) gives an even better agreement (dash-dotted red curve in Fig. 10).

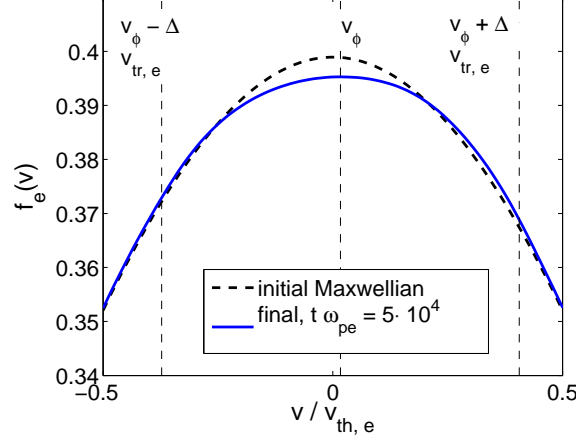


FIG. 9: (color online) Driven IAW case $ZT_e/T_i = 30$. Subthermal electron velocity distribution $f(v)$ at time $t = 5 \cdot 10^4 \omega_{pe}^{-1}$ and position $x/\lambda_{De} = 10.5$ corresponding to the maximum of the electrostatic potential field $\phi(x)$. The wave phase velocity v_ϕ and the location of the separatrices at $v_\phi \pm \Delta v_{tr,e}$ are indicated by vertical fine dashed lines. The initial Maxwellian distribution $f_0(v)$ is shown as a bold dashed line.

2. IAW case $ZT_e/T_i = 10$

In this case, one considers a Hydrogen plasma ($Z = 1$, $m_i/m_e = 1836$) at the temperature ratio $T_e/T_i = 10$, in which an IAW with wavenumber $k\lambda_{De} = 0.3$ is driven up to finite amplitude. Here one expects that the frequency shifts from the trapped electrons and ions will tend to cancel each other (see Fig. 3). The complex frequency from the linear dispersion relation is $\omega_L/\omega_{pe} = 8.032 \cdot 10^{-3} - 2.450 \cdot 10^{-4}i$. The linear damping $\gamma = \Im(\omega_L)$ is dominated by the ion contribution ($\gamma_i/\gamma_e \sim 2$). The real frequency obtained from setting the real part of the linear dispersion to zero is $\omega_{L,r}/\omega_{pe} = 7.989 \cdot 10^{-3}$, *i.e.* somewhat smaller than the real part $\Re(\omega_L)$ of the complex frequency. The analytic approximation to the IAW frequency given in Eq. (22) has the value $\omega/\omega_{pe} = 7.725 \cdot 10^{-3}$. The differences between these three estimates is in fact comparable to the measured frequency shifts.

Fitting the data for the frequencies of the non-linear waves generated in the simulation with $\omega_{NL}^{fit}(\phi_0) = \omega_{NL}^{fit}(0) + C \phi_0^{1/2}$ gives the frequency $\omega_{NL}^{fit}(0)/\omega_{pe} = 7.989 \cdot 10^{-3}$ for $\phi_0 = 0$, *i.e.* the same value as $\omega_{L,r}$ (apparently a coincidence because this relation did not hold true for other values of ZT_e/T_i). The normalized frequency shifts from the simulation, again estimated as $\delta\omega_{NL}^{sim}(\phi_0) = \omega_{NL}^{sim}(\phi_0) - \omega_{NL}^{fit}(0)$, are shown in Fig. 11 and are about half as

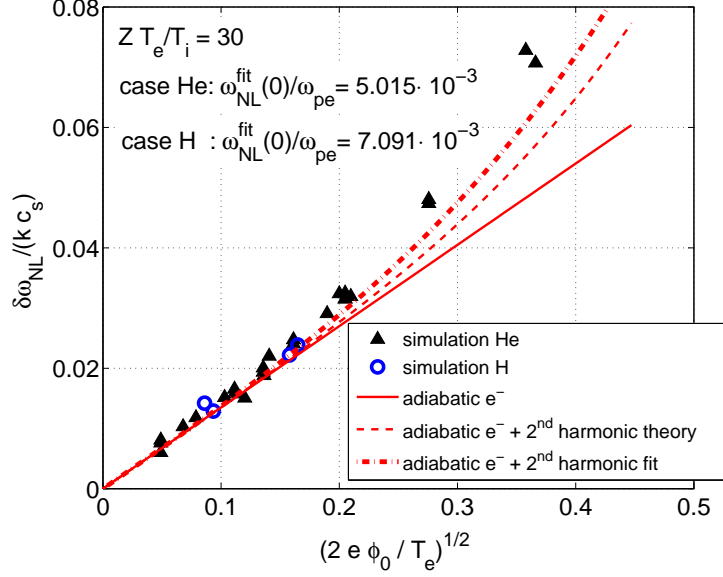


FIG. 10: (color online) Driven IAW case $Z T_e/T_i = 30$. Normalized frequency shifts $\delta\omega_{NL}/(k c_s)$ from the Vlasov simulations [black triangles for Helium (He, $Z/A = 1/2$) and blue circles for Hydrogen (H, $Z/A = 1$)] are shown as a function of $\sqrt{2e\phi_0/T_e}$ along with the theoretical prediction (solid line) assuming adiabatic electron and sudden ion wave generation. In this case of large $Z T_e/T_i$, only the positive electron contribution is in fact significant. The dashed curve includes the frequency shift from the 2^{nd} harmonic theory. The dash-dotted curve uses that theory with the value of ϕ_2 given by the fit to the data shown in Fig. 14.

large as the shifts for the $Z T_e/T_i = 30$ case shown in Fig. 10. The smaller normalized shift results from the fact that the electron and ion contributions are comparable in magnitude but opposite in sign.

Here, a significant difference in the theory curves arises from assuming the ions to follow an adiabatic ($\alpha_i = 0.544$) or a sudden ($\alpha_i = 0.823$) distribution in Eq. (24). Just as large an influence results from the choice of the phase velocity, obtained from the various estimates of the frequency, because of the sensitivity of the exponential term in this equation. For example, choosing the analytic approximation rather than one of the numerical solutions for the frequency makes the negative ion shift ~ 1.5 times larger. There are three theoretical curves plotted in Fig. 11: the solid straight line uses Eq. (24) with the adiabatic choice for both electrons and ions, $\alpha_e = \alpha_i = 0.544$, and the phase velocity $v_\phi/v_{th,i} = 3.608$, corresponding to the frequency $\omega_{L,r} \simeq \omega_{NL}^{fit}(0) = 7.989 \cdot 10^{-3} \omega_{pe}$. The slightly upward curved

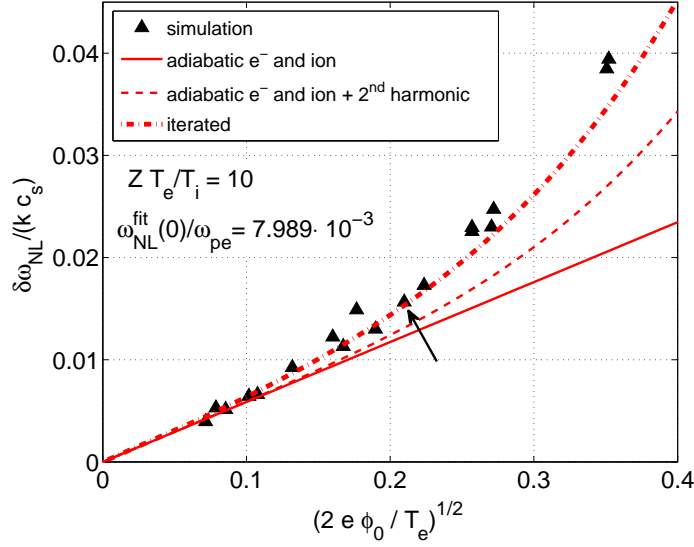


FIG. 11: (color online) Driven IAW case $Z T_e/T_i = 10$. Normalized frequency shifts $\delta\omega_{\text{NL}}/(k c_s)$ from the Vlasov simulations (triangles) are shown as a function of $\sqrt{2e\phi_0/T_e}$ along with the theoretical prediction assuming an adiabatic wave generation for both electrons and ions. The straight solid red curve is obtained from Eq. (24) considering constant phase velocity $v_\phi/v_{\text{th},i} = 3.608$ obtained from $\omega/\omega_{pe} = 7.989 \cdot 10^{-3}$. The dashed (red) curve includes the contribution from the 2nd harmonic. Using an iterative process, one finds the dash-dotted red curve for which the phase velocity is adjusted upward to account for the positive frequency shift as ϕ_0 increases. The data value pointed out with an arrow corresponds to a simulation considered in more detail in Sec IV D.

dashed line is obtained by adding the contribution of the 2nd harmonic frequency shift given by Eq. (33). Because the frequency shift increases the phase velocity, the contribution of the ions to the frequency shift will be less if Eq. (24) is re-evaluated with an updated phase velocity. Using a first order iterative process, one re-evaluates this relation until convergence is achieved. This adjustment lowers the contribution of the negative ion shift and brings the theory and the simulation values for the frequency shift into much better agreement. As in the case $Z T_e/T_i = 30$, the shifts for $\sqrt{2e\phi_0/T_e} \gtrsim 0.2$ obtained from the simulation are thus greater (more positive) than predicted by the kinetic model. These differences can again be assigned to fluid-like non-linear harmonic generation, leading to an additional positive shift contribution at larger wave amplitudes.

3. IAW case $ZT_e/T_i = 6$

In this case, one considers again driven IAWs with wavenumber $k\lambda_{De} = 0.3$ in a Hydrogen plasma ($Z = 1$), but with a temperature ratio $T_e/T_i = 6$. At this low ratio, one expects the negative contribution from ions to dominate the non-linear frequency shift (see Fig. 3). The complex frequency from the linear dispersion relation is $\omega_L/\omega_{pe} = 8.869 \cdot 10^{-3} - 6.671 \cdot 10^{-4}i$. The phase velocity is thus only three times the ion thermal velocity, $v_\phi/v_{th,i} = 3.1$, and linearly the wave is strongly damped, $|\gamma/\omega| = |\Im(\omega_L)/\Re(\omega_L)| = 7.5 \cdot 10^{-2}$. The frequency obtained from solving $\Re[\epsilon_L(\omega_{L,r})] = 0$ is $\omega_{L,r}/\omega_{pe} = 8.535 \cdot 10^{-3}$, significantly smaller than $\Re(\omega_L)$. The analytic approximation (22) to the frequency, $\omega/\omega_{pe} = 8.336 \cdot 10^{-3}$, is yet smaller. In the simulations, the waves are all driven at $\Re(\omega_L)$ with varying driver amplitudes and time durations to obtain different wave amplitudes ϕ_0 .

The normalized frequency shifts $\delta\omega_{NL}/(k c_s)$ from the Vlasov simulation results for $ZT_e/T_i = 6$ are plotted in Fig. 12. Similar to the data presented in the previous sections for higher values of ZT_e/T_i , the simulation frequency shifts are computed relative to the value $\omega_{NL}^{fit}(0) = 8.801 \cdot 10^{-3}$, obtained from fitting the frequencies to a function of the form $\omega_{NL}^{fit}(\phi_0) = \omega_{NL}^{fit}(0) + C\phi_0^{1/2}$. In Fig. 12, the simulation results are compared to the theory estimate Eq. (24) assuming adiabatic electrons and sudden or adiabatic ion wave generation. The theoretical estimate furthermore took $v_\phi/v_{th,i} = 3.08$, corresponding to the frequency of the fit. The adiabatic ion approximation (the red dashed line) clearly disagrees with the data. The sudden ion approximation shown by the straight solid line is a reasonable match. Here, for the amplitudes considered $\sqrt{2e\phi_0/T_e} \lesssim 0.25$, the non-linear fluid-like contribution to the frequency shift from harmonic generation is small. The dashed curve with the harmonic shift added to the sudden ion approximation shows this small difference. The dash-dotted (blue) downward curving line which results from the iterative procedure described previously agrees fairly well with the data.

C. Fraction of trapped electrons and ions in IAWs

The non-linear kinetic frequency shift for IAWs, dependent on competing contributions from both electrons and ions, results from the deformation of the corresponding distributions in the resonant regions. To obtain theoretical estimates of the frequency shifts, distributions

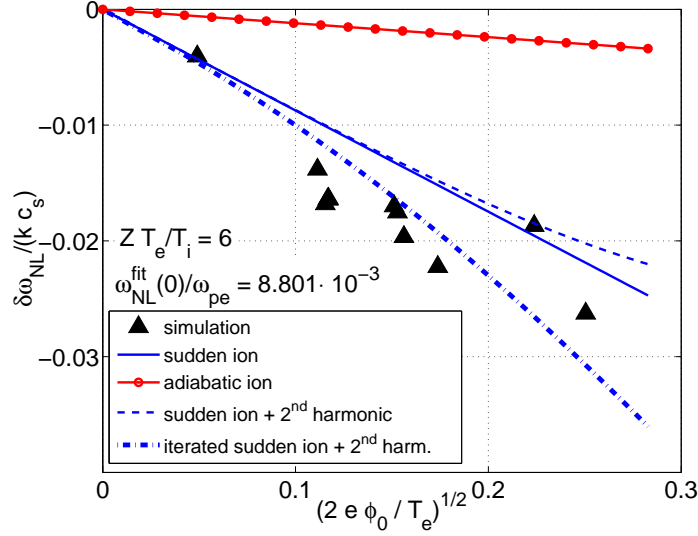


FIG. 12: (color online) Driven IAW case $Z T_e / T_i = 6$. Normalized frequency shifts $\delta\omega_{\text{NL}} / (k c_s)$ from the Vlasov simulations (triangles) are shown as a function of $\sqrt{2e\phi_0/T_e}$ along with the theoretical prediction assuming adiabatic electron and sudden ion (solid straight blue line) and adiabatic ion (dash straight red line) wave generation. The dashed blue line includes the second harmonic contribution from the fluid theory. In this case of low $Z T_e / T_i$, the negative contribution from ions to the frequency shift is dominant. The dash-dotted blue line results from an iterative process that adjusts the phase velocity downward to account for the negative frequency shift as ϕ_0 increases.

for two limiting cases of the wave generation, sudden and adiabatic, have been considered (see Sec. II). One may wonder how well the simulation distributions are actually represented by these limiting forms. Comparing simulation results and theoretical estimates at the level of the frequency shifts only provides an indirect measure for addressing this issue. Comparing the fractions of trapped electrons and ions as a function of the wave amplitude provides a first attempt at a more direct measure. Studying this fraction of trapped particles is addressed here, while the most direct measure of comparing the actual distributions will be addressed in the following section.

Given a finite amplitude electrostatic wave with wavelength λ and potential field $\phi(x, t)$, the fraction of trapped particles for a species with distribution $f(x, v, t)$ at a given time t is defined as

$$\frac{N_{\text{tr}}}{N} = \frac{1}{N \lambda} \int_{-\lambda/2}^{\lambda/2} dx \int_{v_\phi - u_{\text{sep}}(x, t)}^{v_\phi + u_{\text{sep}}(x, t)} dv f(x, v, t), \quad (65)$$

where

$$u_{\text{sep}}(x, t) = \sqrt{\frac{2}{m} \left[\max_x (q\phi(x, t)) - q\phi(x, t) \right]}$$

defines the velocity at the separatrix between trapped and passing particles in the wave frame (\max_x is taken over one wavelength, $-\lambda/2 < x < \lambda/2$).

For the simulation results, Eq. (65) is computed through numerical quadrature of the distribution $f(x_i, v_j, t)$ on the phase space grid (x_i, v_j) after having identified the trapped/passing separatrix based on the numerical electrostatic field $\phi(x_i, t)$ at the same time t .

The theoretical estimates for the trapping fractions can be computed as follows: For the sudden distribution f_s defined by Eq. (9), one has

$$\left(\frac{N_{\text{tr}}}{N} \right)_s = \frac{1}{N\lambda} \int_{\text{tr}} dx dv f_s = \frac{1}{N\lambda} \int_{\text{tr}} dx dv f_0,$$

where f_0 is the initial distribution and $\int_{\text{tr}} dx dv$ stands for the integration over the trapping region as in Eq. (65). For f_0 Maxwellian, one obtains:

$$\left(\frac{N_{\text{tr}}}{N} \right)_s = \frac{1}{2\lambda} \int_{-\lambda/2}^{\lambda/2} dx \left[\text{erf} \left(\frac{v_\phi + u_{\text{sep}}(x)}{\sqrt{2} v_{\text{th}}} \right) - \text{erf} \left(\frac{v_\phi - u_{\text{sep}}(x)}{\sqrt{2} v_{\text{th}}} \right) \right], \quad (66)$$

where $\text{erf}(x) = (2/\sqrt{\pi}) \int_0^x dt \exp(-t^2)$ stands for the error function. Assuming the field $\phi(x)$ to be sinusoidal, one has $u_{\text{sep}}(x) = \Delta v_{\text{tr}} \cos(kx/2)$. If one furthermore expands the distribution f_0 to second order around the phase velocity v_ϕ , as was done for estimating the theoretical frequency shifts in Sec. II, one can carry out the integral over x in (66) analytically to obtain

$$\left(\frac{N_{\text{tr}}}{N} \right)_s \simeq \frac{4}{\pi} \Delta v_{\text{tr}} f_0(v_{\text{th}})/N + \frac{4}{9\pi} \Delta v_{\text{tr}}^3 \frac{d^2 f_0(v_{\text{th}})/N}{dv^2}, \quad (67)$$

where $d^2[f_0(v_{\text{th}})/N]/dv^2$ is given by (13).

For the adiabatic distribution f_a defined by Eq. (10), one has

$$\left(\frac{N_{\text{tr}}}{N} \right)_a = \frac{1}{N\lambda} \int_{\text{tr}} dx dv f_a = \frac{1}{N} \int_{v_\phi - \langle u_{\text{sep}} \rangle_x}^{v_\phi + \langle u_{\text{sep}} \rangle_x} dv f_0,$$

where $\langle u_{\text{sep}} \rangle_x$ stands for the spatial average over one wavelength of the velocity at the separatrix. Considering again f_0 Maxwellian, one can integrate analytically to obtain:

$$\left(\frac{N_{\text{tr}}}{N} \right)_a = \frac{1}{2} \left[\text{erf} \left(\frac{v_\phi + \langle u_{\text{sep}} \rangle_x}{\sqrt{2} v_{\text{th}}} \right) - \text{erf} \left(\frac{v_\phi - \langle u_{\text{sep}} \rangle_x}{\sqrt{2} v_{\text{th}}} \right) \right]. \quad (68)$$

Assuming the field $\phi(x)$ to be sinusoidal, one has $\langle u_{\text{sep}} \rangle_x = (2/\pi)\Delta v_{\text{tr}}$. If one furthermore expands the distribution to second order around v_ϕ , one obtains the approximate relation:

$$\left(\frac{N_{\text{tr}}}{N}\right)_a \simeq \frac{4}{\pi}\Delta v_{\text{tr}} f_0(v_{\text{th}})/N + \frac{8}{3\pi^3}\Delta v_{\text{tr}}^3 \frac{d^2 f_0(v_{\text{th}})/N}{dv^2}. \quad (69)$$

Comparing (67) and (69), one may note that it is only to order $(\Delta v_{\text{tr}}/v_{\text{th}})^3 \sim (q\phi_0/T)^{3/2}$ that the fraction of trapped particles differs between the sudden and adiabatic cases. At low amplitudes, measuring this fraction may not allow one to distinguish between the two types of distributions. More exactly, the *relative* difference between the trapped fractions for the sudden and adiabatic cases can be estimated as:

$$\frac{|(N_{\text{tr}}/N)_s - (N_{\text{tr}}/N)_a|}{(4/\pi)\Delta v_{\text{tr}} f_0(v_{\text{th}})/N} \simeq \left(\frac{1}{9} - \frac{2}{3\pi^2}\right) \left(\frac{\Delta v_{\text{tr}}}{v_{\text{th}}}\right)^2 \left|\left(\frac{v_\phi}{v_{\text{th}}}\right)^2 - 1\right| \simeq 0.17 \frac{q\phi_0}{T} \left|\left(\frac{v_\phi}{v_{\text{th}}}\right)^2 - 1\right|.$$

For ions, this difference is thus amplified by a factor $(ZT_e/T_i)|(v_\phi/v_{\text{th},i})^2 - 1| \simeq (ZT_e/T_i)^2$ compared to electrons (recall that $(v_\phi/v_{\text{th},i})^2 \simeq ZT_e/T_i \gg 1$ and $(v_\phi/v_{\text{th},e})^2 \simeq Zm_e/m_i \ll 1$ in the case of IAWs). The fraction of trapped particles is therefore expected to be a more relevant measure for identifying the type of distribution for the ions than for the electrons.

1. IAW case $ZT_e/T_i = 30$

The fraction of trapped electrons as a function of the wave amplitude obtained from simulations is displayed in Fig. 13 in the simplest IAW case, i.e. when $ZT_e/T_i = 30$ for which ion trapping is essentially negligible. The theoretical predictions in both the sudden and adiabatic wave generation limits and assuming a sinusoidal field are also plotted for comparison. These two limiting cases provide essentially the same estimates over the considered range of amplitudes. Differences between making no approximation on the background distribution, as in Eqs. (66) and (68) respectively, or Taylor expanding to second order around $v = v_\phi$, as in (67) and (69) respectively, are thus negligible as well.

Note in Fig. 13 that for the larger amplitudes considered, $\Delta v_{\text{tr},e}/(\sqrt{2}v_{\text{th},e}) = \sqrt{2e\phi_0/T_e} \gtrsim 0.2$, the fractions of trapped electrons from the simulations fall below the theoretical results. Recall that at these large amplitudes, the frequency shifts from the simulations also deviate from (are larger than) the values predicted by theory (see Fig. 10). Computing the number of trapped particles requires knowledge of the electrostatic field $\phi(x)$ which in general is not sinusoidal. In Fig. 14, the corresponding internal electric field $E_{\text{es}}^{\text{int}} = -\partial\phi/\partial x$ from the

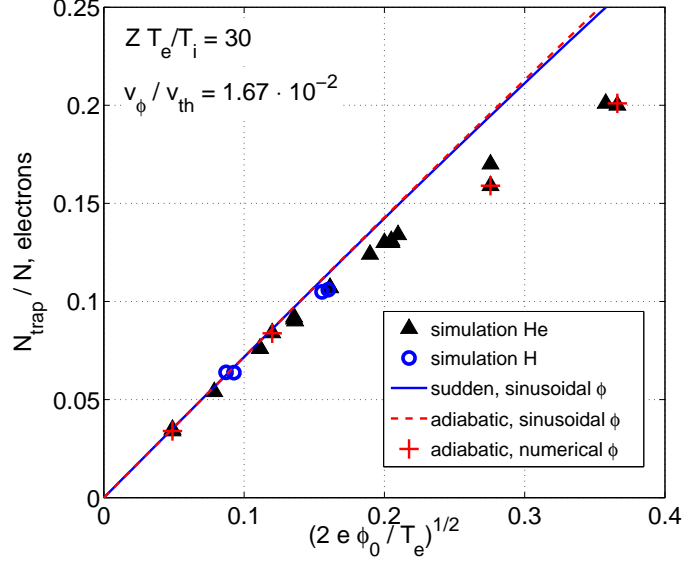


FIG. 13: (color online) Driven IAW case $Z T_e / T_i = 30$. The fraction of trapped electrons from the Vlasov simulations [black triangles for Helium (He, $Z/A = 1/2$) and blue circles for Hydrogen (H, $Z/A = 1$)] is shown as a function of the wave amplitude $\sqrt{2e\phi_0/T_e}$. The theoretical predictions in both the sudden (solid blue line) and adiabatic (dashed red line) wave generation limits and assuming a sinusoidal field are plotted for comparison. The theoretical estimate in the adiabatic limit that uses the electrostatic field from the simulation is also shown for a few simulation cases (red crosses).

simulations is shown as a function of x for a small and a large amplitude wave along with a purely sinusoidal wave for reference. These fields are considered at a time within the BGK-type period of the wave evolution. The shape of the small amplitude wave ($\sqrt{2e\phi_0/T_e} \simeq .05$), for which the number of trapped electrons and the frequency shift agree with the theoretical estimates that assume a sinusoidal wave, confirms this assumption. The large amplitude wave ($\sqrt{2e\phi_0/T_e} \simeq 0.37$) however has a highly distorted waveform resulting from significant harmonic contributions. Computing the fraction of trapped electrons using Eq. (68) with the actual wave field $\phi(x)$ from the simulation, one finds a nearly perfect agreement with the adiabatic theory at all amplitudes, as shown in Fig. 13.

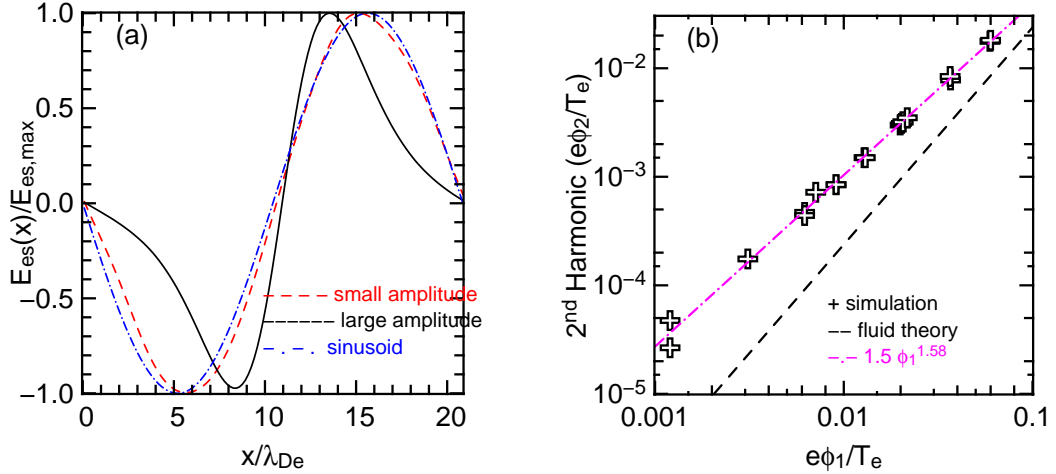


FIG. 14: (color online) Driven IAW case $ZT_e/T_i = 30$. (a) The internal electrostatic field $E_{\text{es}}^{\text{int}}(x)$ from simulations for a small amplitude ($\sqrt{2e\phi_0/T_e} = .05$, dashed line) and large amplitude ($\sqrt{2e\phi_0/T_e} = 0.37$, full line) wave. An exact sinusoid is shown for comparison (dash-dotted). All wave fields are normalized to a maximum of one. (b) The amplitude of the 2nd harmonic ϕ_2 is shown as a function of the fundamental from the simulations (crosses) and (dashed line) from the fluid theory of Sec II B 2. The simulation data is fit best with the power law $\phi_1^{1.58}$

2. IAW case $ZT_e/T_i = 10$

The fractions of trapped ions and electrons for IAWs in the case $ZT_e/T_i = 10$ are shown in Figs. 15.a and 15.b respectively. For a given wave amplitude, the fraction of trapped electrons is much larger than the fraction of trapped ions, since the phase velocity is much smaller than the electron thermal velocity but much larger than the ion thermal velocity (see Figs. 2.a and 2.b). Recall that in this case, the frequency shifts from the electrons and ions are however similar in magnitude.

The theoretical predictions for the trapped ion fraction in both the sudden and adiabatic wave generation limits, for a sinusoidal field, are also plotted for comparison in Fig. 15.a. For small amplitudes, $\Delta v_{\text{tr},i}/(\sqrt{2}v_{\text{th},i}) = \sqrt{2Ze\phi_0/T_i} \lesssim 0.6$, these theoretical estimates for the two limiting cases are essentially identical and in very good agreement with the simulation results. At larger amplitudes, $\sqrt{2Ze\phi_0/T_i} \gtrsim 0.6$, these estimates diverge significantly from each other and their Taylor expansion approximations (67) and (69) become rapidly inaccurate as well, so that the full distribution estimates (66) and (68) have been consid-

ered. At these larger amplitudes, one notes that the simulation values in fact fit neither one of these two theoretical predictions. However, estimating the fraction of trapped ions for an adiabatic distribution using Eq. (68) with the electrostatic field from the simulation, instead of being assumed sinusoidal, leads to a very good agreement with the simulation results for all amplitudes (red crosses in Fig. 15.a). Conversely, the fraction of trapped ions computed with the numerical field in the sudden limit according to Eq. (66) presents very large deviations with the simulation results. These observations lead to the conclusion that the ions are best represented by an adiabatic distribution.

The theoretical predictions for the trapped electron fractions in both the sudden and adiabatic wave generation limits, for a sinusoidal field, have been added for comparison in Fig. 15.b as well. For the amplitudes considered, these estimates are essentially identical in both limiting cases and whether the distribution is Taylor expanded or not is insignificant. As was true for the ions, at low amplitudes, $\Delta v_{\text{tr},e}/(\sqrt{2}v_{\text{th},e}) = \sqrt{2e\phi_0/T_e} \lesssim 0.2$ (corresponding to $\Delta v_{\text{tr},i}/(\sqrt{2}v_{\text{th},i}) = \sqrt{2Ze\phi_0/T_i} \lesssim 0.6$), the simulation results for the electrons are in good agreement with these theoretical curves. At larger amplitudes, $\sqrt{2e\phi_0/T_e} \gtrsim 0.2$, the simulation results drop below the theoretical curves, in a similar way and for similar amplitudes as for $ZT_e/T_i = 30$ (see Fig. 13). However, if the fields from the simulations are used in Eq. (68) for the theoretical estimates in the adiabatic limit, these corrected predictions accurately match the fractions of trapped electrons from the simulations at all amplitudes, as shown in Fig. 15.b. All these results for the ion and electron fractions are consistent with the frequency shift dependence on wave amplitude shown in Fig. 11, in that the simulations are fit best by the adiabatic ion and the adiabatic electron distributions.

3. IAW case $ZT_e/T_i = 6$

Lastly, the fractions of trapped particles for $ZT_e/T_i = 6$ is considered. Recall that in this case, the frequency shift is predominately set by the ions and therefore is negative. The fractions of trapped ions and electrons, integrated from the simulation results during the same time intervals that the frequency shifts are computed, are shown respectively in Figs. 16.a and 16.b. Over the amplitude range considered in these simulations, i.e. $\Delta v_{\text{tr},e}/(\sqrt{2}v_{\text{th},e}) = \sqrt{2e\phi_0/T_e} \lesssim 0.25$ corresponding to $\Delta v_{\text{tr},i}/(\sqrt{2}v_{\text{th},i}) = \sqrt{2Ze\phi_0/T_i} \lesssim 0.6$, the fractions of trapped ions agree well with the theoretical prediction for the sudden

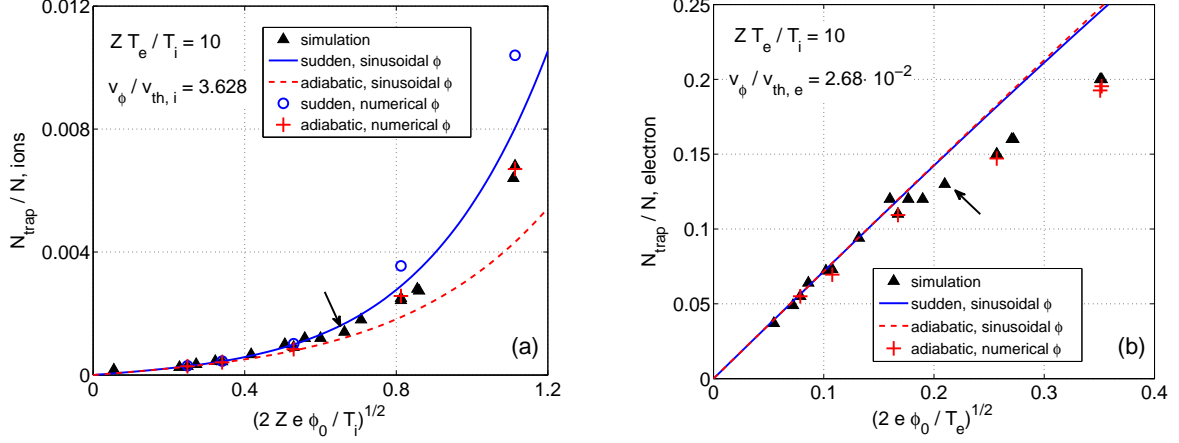


FIG. 15: (color online) Driven IAW case $ZT_e/T_i = 10$. The fraction of trapped (a) ions and (b) electrons from the Vlasov simulations (black triangles) is shown as a function of the wave amplitude $\sqrt{2eZ\phi_0/T_i}$ and $\sqrt{2e\phi_0/T_e}$ respectively. The theoretical predictions in both the sudden (solid blue line) and adiabatic (dashed red line) wave generation limits with a sinusoidal field are plotted for comparison. The theoretical estimate in both the sudden (blue circles) and adiabatic limit (red crosses) that use the electrostatic field from the simulation is also shown for a few simulation cases.

distribution with a sinusoidal field (theoretical results with or without Taylor expansion of the distribution around v_ϕ are essentially identical here), as shown in Fig. 16.a. The fractions of trapped electrons however agree well with either the sudden or the adiabatic theoretical estimates because, over the simulated amplitude range, these distributions have the same trapping fractions, as shown in Fig. 16.b. Note that for this case $ZT_e/T_i = 6$, the largest wave amplitudes considered are just at the critical value where, due to the appearance of non-negligible harmonic components, the fractions of trapped electrons from the simulations start to fall below the theoretical values for a sinusoidal field, as was already clearly seen for larger ZT_e/T_i (see Figs. 13 and 15.b). These results for the trapping fractions in the case $ZT_e/T_i = 6$ confirm the observations made with respect to the corresponding frequency shifts, in particular concerning the ion distributions which appear to be best represented by the sudden limit.

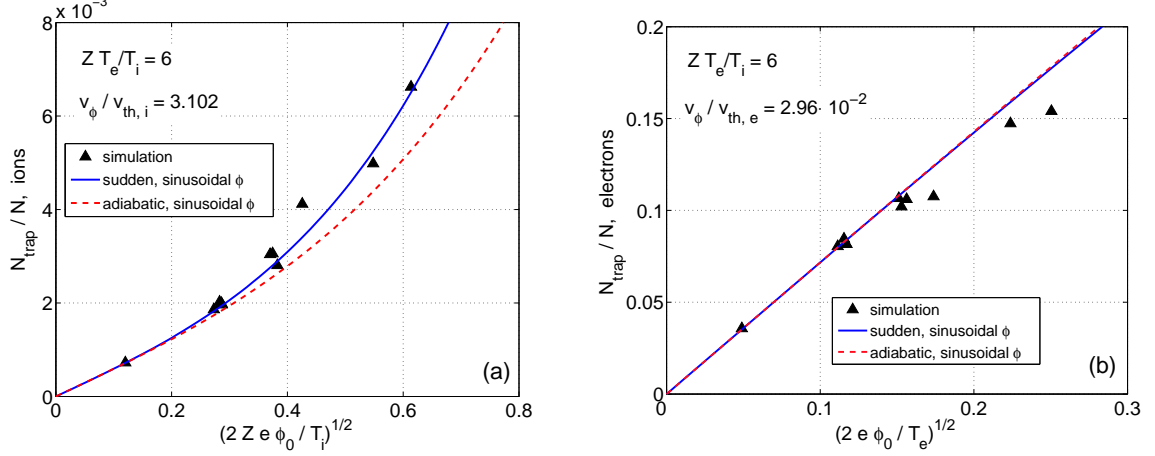


FIG. 16: (color online) Driven IAW case $ZT_e/T_i = 6$. The fraction of trapped (a) ions and (b) electrons from the Vlasov simulations (black triangles) is shown as a function of the wave amplitude $\sqrt{2eZ\phi_0/T_i}$ and $\sqrt{2e\phi_0/T_e}$ respectively. The theoretical predictions in both the sudden (solid blue line) and adiabatic (dashed red line) wave generation limits with a sinusoidal field are plotted for comparison.

D. Distribution in Resonant Region as Function of Energy

In the previous section, the analysis of the trapped ion and electron fractions in the case of IAWs provided some confirmation of the agreements that were found between the simulation results for the frequency shifts and the theoretical predictions, in particular concerning whether the ion distribution is best fit by the sudden or adiabatic limit. Studying these fractions also clearly pointed out that the assumption of purely sinusoidal wave fields is a limitation of the kinetic model used for estimating the non-linear frequency shifts that result from trapping, as it is unable to provide accurate predictions for larger amplitude waves which develop harmonic components, i.e. typically for $\sqrt{2e\phi_0/T_e} \gtrsim 0.25$ in the case of IAWs. Further insight and confirmation of the observations based on the frequency shifts and trapping fractions will now be provided for IAWs by actually studying the particle distributions in the resonant regions of phase space, i.e. for particles with velocities near the phase velocity v_ϕ .

Once the non-linear wave has reached a BGK-like state, the particle distributions are functions of the constants of motion in the wave frame, *i.e.* energy $W = m(v - v_\phi)^2/2 + q\phi(x)$ and, for passing particles only, the sign $\sigma = \text{sgn}(v - v_\phi)$ of the wave frame velocity along x .

This is clearly illustrated for example by the two limiting cases, sudden and adiabatic, in Eqs. (9) and (10). To compare the simulation results to these theoretical distributions requires computing $f(W, \sigma)$ from the numerical distribution $f(x_i, v_j)$ given on the Cartesian phase space mesh (x_i, v_j) and using as well the numerical electrostatic field $\phi(x_i)$. Note that within the BGK-like phase, the so-obtained function $f(W, \sigma)$ should be essentially independent of the time t at which the distribution $f(x_i, v_j)$ is considered. Constructing $f(W, \sigma)$ is achieved by first computing the energy $W_{ij} = m(v_j - v_\phi)^2/2 + q\phi(x_i)$ at each phase space grid point, having chosen an appropriate estimate of the phase velocity v_ϕ [typically one estimates $v_\phi = \omega_{NL}^{fit}(0)/k$]. The distribution $f(W, \sigma)$ of a given species is then evaluated with the following binning procedure: The corresponding energy range for resonant particles, *i.e.* $\min_x(q\phi_0) < W < \max_x(q\phi_0)$ for trapped and $\max_x(q\phi_0) < W \lesssim 2 \max_x(q\phi_0)$ for passing particles, is divided into bins centered at W_b and with widths ΔW_b . For an energy W_b within the trapping range, one then simply computes the average

$$f(W_b) \simeq \frac{1}{N_b} \sum_{W_{ij} \in \text{bin}(W_b)} f(x_i, v_j),$$

where N_b stands for the number of phase space points (x_i, v_j) whose corresponding energy W_{ij} lies in the bin centered at W_b , referred to as $\text{bin}(W_b)$. For energies W_b in the untrapped range, one distinguishes between forward ($\sigma = +1$) and backward passing ($\sigma = -1$) according to the sign of the wave frame velocity:

$$f(W_b, \sigma) \simeq \frac{1}{N_b} \sum_{W_{ij} \in \text{bin}(W_b) \ \& \ \text{sgn}(v_j - v_\phi) = \sigma} f(x_i, v_j),$$

where N_b again stands for the number of phase space points (x_i, v_j) contributing to the sum. The widths ΔW_b of the bins are chosen as narrow as possible while still ensuring sufficient statistics from corresponding phase space points (x_i, v_j) for accurately estimating the averages in the above relations. If the phase space mesh (x_i, v_j) is taken equidistant, the widths ΔW_b thus need to be taken wider for higher energy levels W_b : $\Delta W_b \sim \{2m[W_b - \min_x(q\phi_0)]\}^{1/2} \Delta v$, where Δv is the width of the velocity mesh.

In the following illustration, the numerical distributions of particles are compared to the theoretical predictions in the sudden and adiabatic limits. These limiting distributions are provided by relations (9) and (10) which have been evaluated using the exact Maxwellian distribution f_0 [no Taylor expansion as in Eq. (11)] with either a sinusoidal wave field

$\phi(x) = \phi_0 \cos(kx)$ or the numerical field $\phi(x)$ provided by the simulation. Note that the average velocity \bar{u} appearing in Eq. (10) can be derived analytically for sinusoidal waves, giving for passing particles ($0 < \kappa < 1$):

$$\bar{u}(\kappa) = \frac{2}{\pi} \frac{\Delta v_{\text{tr}}}{\kappa} E(\kappa^2),$$

and for trapped ($1 < \kappa < \infty$):

$$\bar{u}(\kappa) = \frac{2\Delta v_{\text{tr}}}{\pi} \left[E\left(\frac{1}{\kappa^2}\right) + \left(\frac{1}{\kappa^2} - 1\right) F\left(\frac{1}{\kappa^2}\right) \right],$$

where $\kappa^2 = 2|q|\phi_0/(W + |q|\phi_0)$ is a transformed energy variable and $F(m)$ and $E(m)$ of argument m are the complete elliptic integrals of the first and second kind respectively (see definition after Eq. (12)). All other aspects of evaluating Eqs. (9) and (10) need to be performed numerically.

Distributions shall now be studied for an IAW in the case with $ZT_e/T_i = 10$ (Hydrogen plasma, $Z/A = 1$). Because the frequency shifts from the electrons and the ions are in opposite directions and of similar magnitudes in this case, deviations of the distributions from the adiabatic or sudden limits are particularly important in determining the sign of the total shift.

It is instructive to consider the specific example of the IAW with amplitude $\sqrt{2e\phi/T_e} = 2.2 \cdot 10^{-1}$ ($\sqrt{2q\phi/T_i} = 7.0 \cdot 10^{-1}$), driven slowly over the time interval $t_{\text{drive}} \simeq 5 \cdot 10^4 \omega_{pe}^{-1}$ that corresponds to the data value pointed out with an arrow in Figs. 11, 15.a, and 15.b. The simulated distributions of electrons and ions in the resonant regions are shown in Fig. 17 along with the sudden and adiabatic distributions from theory. As expected, the difference between the theoretical distributions obtained with the field from the simulations and the ones assuming a purely sinusoidal field are significant here. The electrons are very well represented by the adiabatic distribution with the numerical field and clearly distinct from the sudden distribution. Because the electron bounce frequency is very fast on the time scale of IAW growth, the electron distribution has no noticeable filamentary structure in energy and thus matches the adiabatic distribution very well, especially when the potential field ϕ is taken from the simulation rather than assumed to be a pure sinusoid. Thus, contrary to the fraction-of-trapped-electron measurement, which did not differentiate between the sudden and adiabatic limits (see Fig. 15.b), diagnosing the actual distribution unambiguously confirms the adiabatic response.

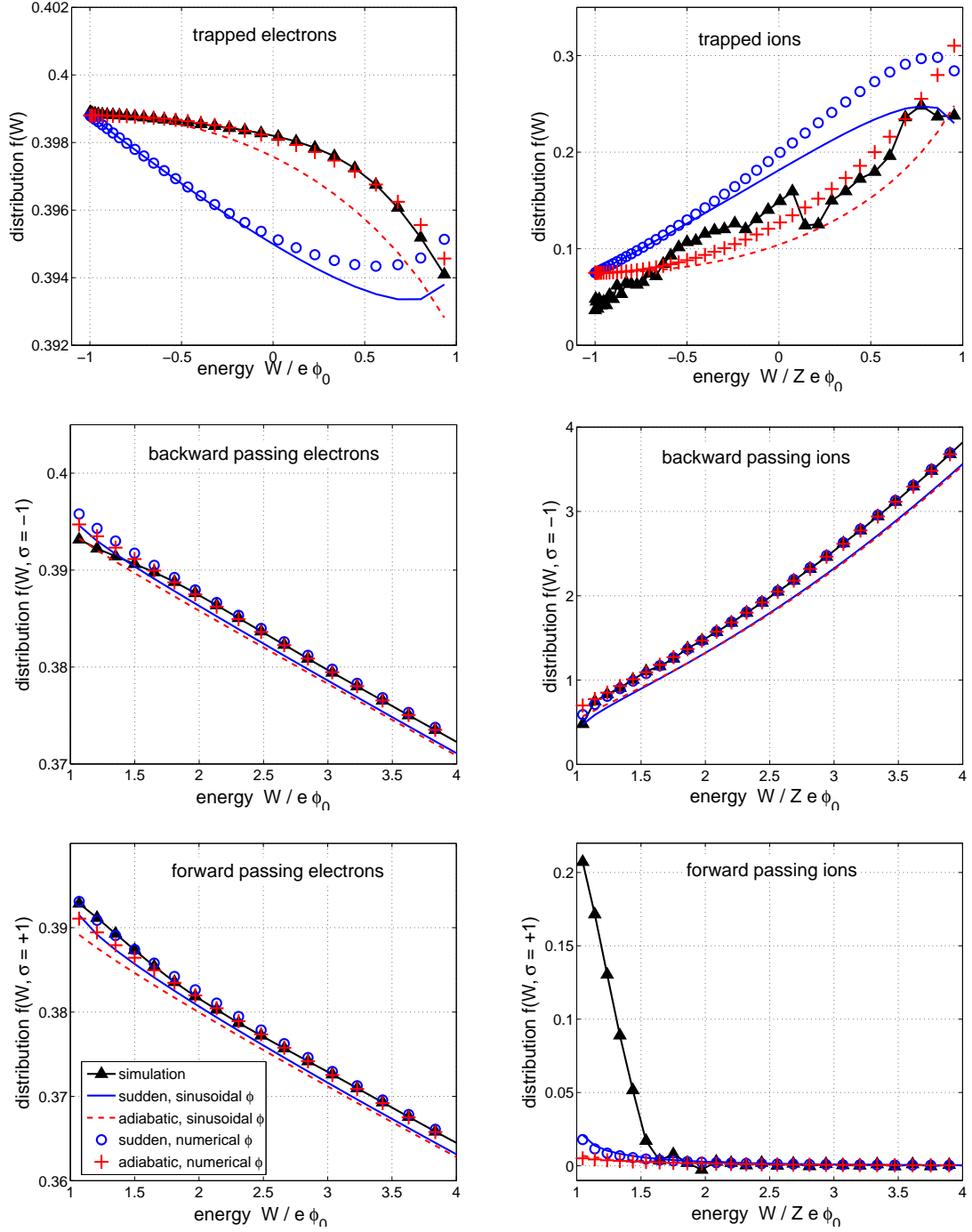


FIG. 17: (color online) Driven IAW case $ZT_e/T_i = 10$ with amplitude $\sqrt{2e\phi/T_e} = 2.2 \cdot 10^{-1}$ (pointed out with an arrow in Figs. 11, 15.a, and 15.b). The electron and ion distribution functions at time $t = 7 \cdot 10^4 \omega_{pe}^{-1}$ as a function of the particle energy in the trapping regions. The distributions for the sudden and adiabatic approximations with the purely sinusoidal field and the field from the simulation are also shown.

The trapped ion distribution is not as smooth as for electrons but is nonetheless consistent with an adiabatic distribution, with a clearly improved match when the numerical fields are used. This study of the distributions for $ZT_e/T_i = 10$ thus supports the frequency shift analysis: both electrons and ions are best represented by the adiabatic model. Near the separatrix, the trapped ions present a slightly lower phase space density than the adiabatic distribution, while the forward-passing untrapped ions present a larger density than the adiabatic or sudden distributions. These deviations essentially remove the discontinuities in the theoretical distributions at the separatrix between the trapped and passing domains and result from the amplitude modulations of the wave before it settled to its BGK-like state. Wave amplitude modulation indeed leads to a redistribution of ions, as originally backwards passing particles, 'carrying' high phase space density, get trapped as the wave amplitude increases and then get partly untrapped as forward passing particles as the wave amplitude decreases, resulting in their effective acceleration.

V. MODELING THE DRIVEN ION ACOUSTIC WAVE

A very simple model for the evolution of a driven ion wave retrieves at least the qualitative behavior of the internal electrostatic complex wave amplitude $\hat{E}_k(t)$. Assuming only the electrons are driven, one solves the equation,

$$\left(\frac{\partial}{\partial t} + \nu + i\delta\omega_{\text{NL}} \right) \hat{E}_k = \frac{1}{2} \frac{\omega^{\text{ext}}}{[1 + (k\lambda_{De})^2]} E_0^{\text{ext}}(t), \quad (70)$$

where ω^{ext} and $E_0^{\text{ext}}(t)$ are respectively the external driver frequency and its time varying amplitude, while ν stands for the Landau damping rate. The frequency ω^{ext} is usually chosen to be the linear resonant frequency from a solution to the kinetic dispersion relation. The frequency shift $\delta\omega_{\text{NL}}$ to the ion acoustic wave is given by Eq. (24) if the wave amplitude reaches a steady state. If the model is successful, the amplitude $|\hat{E}_k(t)|$ and the corresponding frequency shift $\delta\omega_{\text{NL}}$ will be the same as in the Vlasov simulations.

The damping rate $\nu = \sum_j \nu_j$, where j is the species index, is initially chosen to be the linear Landau rate ν_L but decreases with time as particles become trapped. Similarly, the non-linear frequency shift is only established over a time interval of the order of the bounce period of the trapped particles. Several such models have been proposed [7, 13, 14, 23, 31] for the time evolution of the frequency shift and damping rate. Exploring the relative value of

these different models is beyond the scope intended for this paper; consideration is therefore limited to a model developed for ion trapping by Divol and Williams.[7] In this model, the equations for the frequency shift and damping rate from each species j are:

$$\partial_t \delta_j^3 = H(v_{tr,j} - \delta_j) \frac{\omega_{b,j}}{2\sqrt{2\pi}} v_{tr,j}^3 \quad (71)$$

$$\delta\omega_e = \alpha_e \frac{kc_s}{2\sqrt{2\pi}} \frac{\delta_e}{v_{th,e}} \quad (72)$$

$$\delta\omega_i = -\alpha_i \frac{kc_s}{2\sqrt{2\pi}} \Gamma \frac{\delta_i}{v_{th,i}} \quad (73)$$

$$\delta\omega_{NL} = \delta\omega_e + \delta\omega_i + \delta\omega_{harm} \quad (74)$$

$$\nu_j = \nu_{L,j} H(v_{tr,j} - \delta_j). \quad (75)$$

Here, $\Delta v_{tr,j} = 2\sqrt{eZ_j\phi/m_j}$ is the instantaneous trapping width, $\Gamma = (ZT_e/T_i)(v^2 - 1)\exp(-v^2/2)|_{v=v_\phi/v_{th,i}}$, and $H(w)$ once again stands for the Heaviside function. The parameter δ_j represents the actual width of the plateau in velocity space created by particle trapping. If δ_j equals $v_{tr,j}$, the kinetic part $\delta\omega_j$ of the frequency shift is given by Eq. (24). The plateau width, δ_j , will increase at the bounce frequency rate $\omega_{b,j} = \sqrt{|Z_j e k \hat{E}_k|/m_j}$ as long as the wave amplitude does and thereby increase the frequency shift from each species. In addition to the kinetic shift, an instantaneous shift, $\delta\omega_{harm}$, from the IAW harmonics (see Eq. 34) is added.

When the ions and electrons both contribute to the non-linear frequency shift, that is for $ZT_e/T_i \lesssim 10$, the frequency shift of the driven wave after the pump is turned off is the sum of the ion and electron shifts with the ion coefficient between the sudden and adiabatic values. Because the ion bounce period is much longer than the electron one, the growth time can be shorter than the ion bounce period. One thus expects the ion frequency shift to lag the wave amplitude. This feature is caught through Eqs. (70) and (73). In equation (70), the frequency shift and the damping rate are the sum of the time dependent electron and ion contributions. An interesting outcome of the fact that the ion frequency shift may lag the electron one is that there are three epochs: (1) the early time where the electron shift rapidly develops, (2) an intermediate epoch, initiated after approximately one ion bounce period, where the ion shift reduces the total shift (leading to faster growth), and (3) the final epoch where the asymptotic shifts are achieved in a quasi-steady state.

In the simplest case, $ZT_e/T_i = 30$, the ions play little role in the non-linear response. Two examples of the time history according to the model are shown in Fig. 18 along with

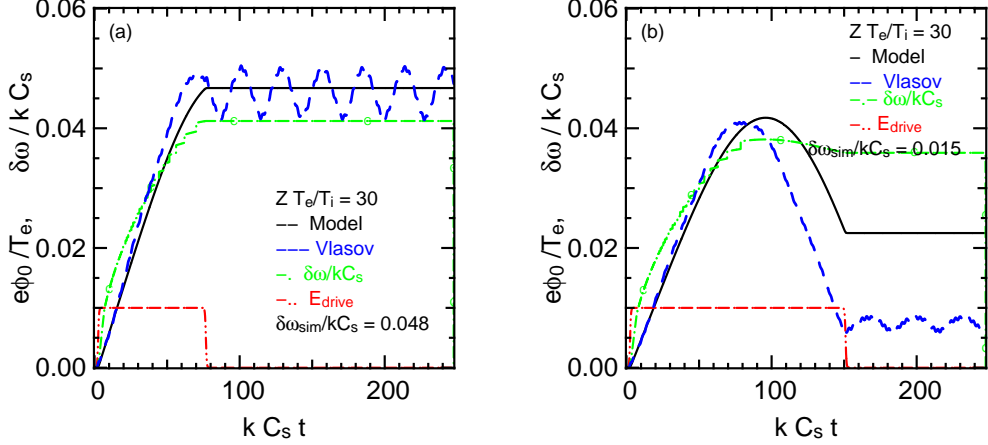


FIG. 18: (color online) The time history of the wave amplitude according to the model equations (black curve) and from the Vlasov simulation (blue dashed curve) for the parameters $ZT_e/T_i = 30$ and $k\lambda_{de} = 0.3$. Also shown is the time dependence of the driver E_0^{ext} as well as the model's frequency shift $\delta\omega_{\text{NL}}$. For the model curve, the parameter α_e was chosen equal to the adiabatic value 0.544, as suggested by results in Fig. 10. In the above plots, the driver amplitude is normalized to a maximum of 0.01 for convenience of illustration. (a) $E_0^{\text{ext}} = 5 \cdot 10^{-4}$ for $\omega_a t < 74$ and $E_0^{\text{ext}} = 0$ afterwards. (b) $E_0^{\text{ext}} = 4 \cdot 10^{-4}$ for $\omega_a t < 150$ and $E_0^{\text{ext}} = 0$ afterwards.

the Vlasov simulation results for the same parameters. Note that the simulations show an oscillation in the wave amplitude after the driver turns off with period about equal to the ion bounce time, an effect not caught in the simple model. This oscillation arises from the exchange of energy between the trapped ions and the wave because the ions have not completely phase-mixed. In the example shown in Fig. 18.a, the wave in the simulation attains its peak value as the driver is turned off at $t = 74 \omega_{pe}^{-1}$. In the model, the frequency shift and the wave amplitude also reach their peak values at this time. The model has about the same amplitude as the Vlasov simulation. In the second example shown in Fig. 18.b, the driver is left on after the wave amplitude reaches its peak value and gets out of phase with the wave whose amplitude then drops to a lower value. The model also reproduces that behavior but the wave amplitude after the driver is turned off is more than twice the amplitude from the simulation.

The time history of the field amplitude is more complicated in cases where both the ions

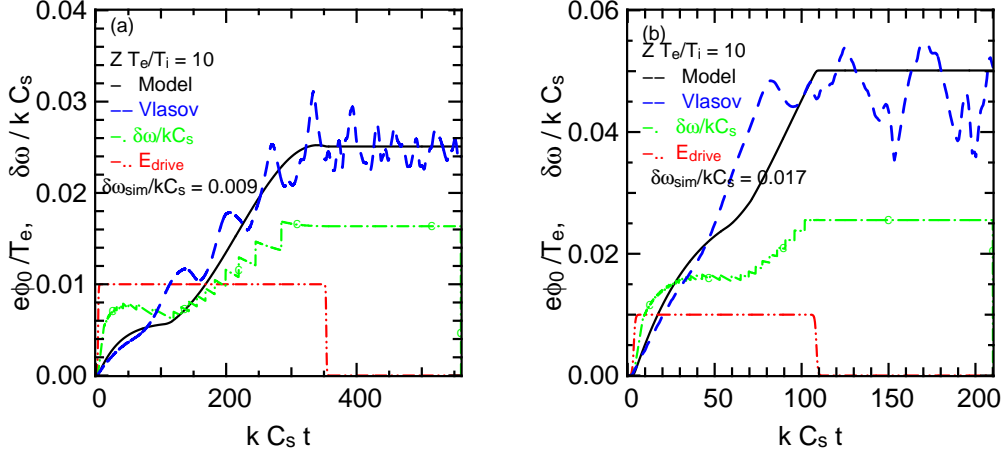


FIG. 19: (color online) Similar to Fig. 18 but for $Z T_e/T_i = 10$. For the model curve, both α_e and α_i were chosen to be equal to the adiabatic value $\alpha = 0.544$, as suggested by results in Fig. 11. (a) $E_0^{\text{ext}} = 1 \cdot 10^{-4}$ for $\omega_a t < 350$ and $E_0^{\text{ext}} = 0$ afterwards. (b) $E_0^{\text{ext}} = 5 \cdot 10^{-4}$ for $\omega_a t < 110$ and $E_0^{\text{ext}} = 0$ afterwards.

and the electrons contribute to the damping and frequency shift. To illustrate this scenario, a hydrogen plasma with $Z/A = 1$, $T_e/T_i = 10$, and $k\lambda_{De} = 0.3$ is considered. One first studies a wave weakly driven over a long time such that the steady state frequency shift from the simulation is close to the one given by adiabatic ions and electrons as shown in Fig. 19.a. In the model and the simulation, there is an intermediate "saturation" in the wave amplitude after the electrons have been trapped ($\omega_a t = 75$ and $\omega_{be} t \simeq 300$) but the ions have just executed one trapping cycle ($\omega_{bi} t = 2\pi$). In the Vlasov simulation, the wave grows after this time with clear oscillations at the slowly decreasing ion bounce period until the driver turns off. In the model the growth resumes as well as the ions become trapped because the total frequency shift decreases (sum of negative ion shift and positive electron shift). The resumed growth traps more electrons which arrests the decrease in the frequency shift. After the driver is off, the wave amplitude in the model is about the same as in the Vlasov simulation but the frequency shift is larger than the Vlasov one.

The model has also been compared to the evolution of the wave driven by a larger external field over a shorter period of time in the second example shown in Fig. 19. In this case, the trapped ions have only executed 2-4 cycles when the driver is turned off whereas the

electrons have executed many. Nonetheless, according to Fig. 11, an adiabatic ion response best reproduces the frequency shift in the simulations. In Fig. 19.b, the model's amplitude in steady state with adiabatic electron and ion response is again similar to the one in the simulation and the frequency shift is again larger.

The reduced fluid model presented in this section is thus useful for qualitative interpretation of the simulations but fails quantitatively in most cases even for the simple systems presented above. In more complicated systems, *e.g.* many wavelengths long or multidimensional, the validity of such reduced models for representing intrinsically kinetic effects is uncertain.

VI. CONCLUSIONS

By making use of the spatially one-dimensional Vlasov code SAPRISTI, we have in this paper systematically compared the theory by Morales, O'Neil and Dewar [42, 43] for kinetic non-linear frequency shifts $\delta\omega_{\text{kin}}$ resulting from particle trapping to simulation results in the case of both EPWs and IAWs. To our knowledge, this is the first thorough study of such frequency shifts for IAWs. Examples focused on parameters of interest to stimulated Raman and Brillouin scattering in recent ICF experiments.[33–35]

It was shown that, within its limits of applicability, i.e. at low amplitudes, $e\phi_0/T_e \ll 1$, the kinetic theory model that predicts a the shift with amplitude scaling as $\phi_0^{1/2}$ as originally derived for EPWs, is valid for IAWs as well.

In the EPW case, both initial value standing waves, as well as slowly-driven propagating waves were generated and compared to the two limiting theoretical cases, 'sudden' and 'adiabatic' respectively, as originally addressed by Dewar [43]. Simulation results showed good agreement of the frequency shift, which is negative in this case of EPWs, with these two limits, confirming a more negative frequency shift for the 'sudden' than for the 'adiabatic' case.

In the IAW case, both electrons and ions contribute to the non-linear kinetic frequency shift, $\delta\omega_{\text{kin}} = \delta\omega_{\text{kin,e}} + \delta\omega_{\text{kin,i}}$, and their contributions have opposite sign: positive for electrons, $\delta\omega_{\text{kin,e}} > 0$, and negative for ions, $\delta\omega_{\text{kin,i}} < 0$. The relative importance of these two contributions depends mainly on the effective temperature ratio ZT_e/T_i with a minor dependence on $k\lambda_{De}$ and essentially no dependence on Zm_e/m_i . Thus, for very large values

of the temperature ratio ZT_e/T_i , the kinetic frequency shift is dominated by the positive electron contribution, at intermediate values, $ZT_e/T_i \simeq 10$, the electron and ion contributions basically compensate each other, while for $ZT_e/T_i < 10$ the negative ion contribution dominates.

At larger amplitudes, for both EPWs and IAWs, simulation results differ progressively more strongly from the standard theoretical estimate for the non-linear kinetic frequency shift. A more detailed analysis revealed the significant role of Fourier harmonic generation that leads to wave steepening as well as to an associated frequency shift. Such a harmonic-related frequency shift, $\delta\omega_{\text{NL,harm}}$, scaling with amplitude as ϕ_0^2 , was derived for IAWs from linearized fluid equations. Adding $\delta\omega_{\text{harm}}$ to the kinetic frequency shift component $\delta\omega_{\text{kin}}$ brought the theory into good agreement with simulation results, even at higher wave amplitudes, for basically all regimes of ZT_e/T_i . Similar agreement at higher amplitudes between simulation results and a total theoretical estimate $\delta\omega_{\text{NL}} = \delta\omega_{\text{kin}} + \delta\omega_{\text{harm}}$ for the EPW frequency shift was achieved as well.

For IAWs, reconstructions of the electron and ion trapping fractions, as well as wave frame energy distributions, provided a more detailed comparison of the simulation results with the two theoretical limits for the wave generation, 'sudden' and 'adiabatic'. These comparisons confirmed the agreements obtained for the frequency shifts between simulation and theoretical estimates in these limiting cases. Thus electrons in slowly driven IAWs, as expected, follow very closely the adiabatic distribution, as their bounce frequency $\omega_{b,e}$ is very large compared to the rate of increase $d \log(\phi_0)/dt$ of the wave amplitude. For ions, the corresponding bounce frequency $\omega_{b,i}$ is significantly smaller (by a factor $\sqrt{Zm_e/m_i}$) than for electrons. Thus, whether the ion distribution and the corresponding kinetic frequency shift will be best represented by the 'adiabatic' or the sudden 'limit' will depend on whether $\omega_{b,i}$ is nonetheless larger or not than the rate $d \log(\phi_0)/dt$. The more detailed analysis of the simulation results further confirmed the significant presence of Fourier harmonics at larger wave amplitudes and how they lead to important distortions of the distributions of resonant particles. This observation reflects the need for a more complete theory, accounting for harmonic effects in a kinetic framework. Such a unified theory appears still to be lacking.

The fully multi-species kinetic simulations of finite amplitude IAWs presented in this paper, clearly point out the important role of resonant wave-particle interactions even for the lighter electrons, effects which are absent when considering the commonly used Boltzmann

response for this lighter species, as already noted in Ref. [2, 3]. Carrying out such multi-species simulations over the slow IAW time scales while resolving the fast dynamics of electrons is however very costly and may become prohibitive when considering larger systems (multi-wavelength long or even multi-dimensional). The need for improved reduced electrons models, beyond the simple Boltzmann model, accounting for certain trapping effects are thus needed.

The effect collisions and side-loss (neglected in these 1D in space and velocity simulations) may have on the de-trapping of electrons and ions in an IAW is considered in Appendix A. Both collisional drag as well as parallel and transverse (to the incoming velocity) diffusion were considered. Side-loss detrapping, resulting from the motion of particles transverse to the direction of propagation of the wave and thus leaving the finite width envelope of the wave was also considered. In general, for a detrapping mechanism to significantly affect the non-linear kinetic frequency shift, the corresponding characteristic detrapping time τ_{detrap} must be comparable or shorter than the typical bounce period $\tau_b = 2\pi/\omega_b$ of a trapped particle. It is shown in Appendix A that these effects must be considered for small wave amplitudes: Eq. (A1) gives the condition for sideloss and Eq. (A12) for collisional detrapping. For typical ICF plasmas, collisions impose a more stringent limit on IAWs than sideloss. However, only the lowest amplitude cases considered in this paper may be affected.

Appendix A: Detrapping mechanisms

The non-linear kinetic frequency shifts, which result from particles trapped in the electrostatic potential troughs of the longitudinal plasma waves, may be reduced or fully eliminated in the presence of detrapping mechanisms. Under laser-fusion relevant conditions, two main detrapping effects need to be considered: 1) Collisions, which may remove particles from the trapping region in velocity space, characterized by $v_\phi - \Delta v_{\text{tr}} < v_x < v_\phi + \Delta v_{\text{tr}}$, where v_x is the velocity component of a particle parallel to the direction of propagation Ox of the longitudinal wave with phase velocity v_ϕ . In general, collisional drag as well as parallel and transverse (to the incoming velocity) diffusion need to be considered. 2) Side-loss detrapping, resulting from the motion of particles transverse to the direction of propagation of the wave and thus leaving the finite width envelope of the wave. In laser-fusion plasmas, the incident light indeed filaments into small speckles because of natural and deliberately-

introduced spatial phase nonuniformities and the plasma waves driven through parametric instabilities in these high intensity regions have similar finite width.

These detrapping mechanisms have been neglected in the simulations presented in this paper and would have required considering a higher dimensional phase space than the 1+1 -dimensional space (x, v_x) used here. Indeed, collisional effects represented by a Landau-type operator require at least one additional velocity space direction v_\perp , perpendicular to the direction of propagation, to correctly account for pitch angle scattering (transverse diffusion), and that thus results in a 1+2 -dimensional phase space simulation. An accurate modeling of side-loss effects in turn requires an additional configuration space dimension y and associated velocity dimension v_y for representing the finite transverse width of the mode, and that thus results in a 2+2 -dimensional simulation. Accounting simultaneously for both collisional and side-loss detrapping would in fact require a 2+3 -dimensional phase space.

Side-loss effects in 2+2 -dimensional collisionless Vlasov simulations have recently been systematically studied in the case of EPWs using the Eulerian-based LOKI code [30]. Although similar simulations, possibly also including collisional effects, may be carried out in the future for IAWs, we shall limit ourselves here to theoretical estimates for the importance of detrapping. In general, for a detrapping mechanism to significantly affect the non-linear kinetic frequency shift, the corresponding characteristic detrapping time τ_{detrapp} must be comparable or shorter than the typical bounce period $\tau_b = 2\pi/\omega_b$ of a trapped particle:

$$\tau_{\text{detrapp}}\omega_b < 2\pi,$$

where the bounce frequency ω_b is estimated by the relation for deeply trapped particles: $\omega_b = k(q\phi_0/m)^{1/2}$.

a. Side-loss Detrapping in an IAW

The characteristic time $\tau_{\text{s.l.}}$ for side-loss of a given species is estimated as $\tau_{\text{s.l.}} = \Delta y/v_{\text{th}}$, where Δy is the transverse width of a laser speckle. Given the f -number and wavelength λ_0 of the laser beam associated to the speckle, the transverse width is of order $\Delta y = f\lambda_0$. One thus obtains:

$$\tau_{\text{s.l.}}\omega_b \simeq \frac{\Delta y}{v_{\text{th}}}\omega_b \simeq k\Delta y\sqrt{\frac{q\phi_0}{T}} \simeq 4\pi f\sqrt{\frac{q\phi_0}{T}}, \quad (\text{A1})$$

where the estimate $k = 2k_0$ for the wavenumber k of the IAW, valid for SBS, and the laser wavenumber $k_0 = 2\pi/\lambda_0$ has been used.

For electrons, side-loss thus becomes significant, i.e. $\tau_{s,l}\omega_{b,e} < 2\pi$, only for sufficiently low wave amplitudes such that $e\phi_0/T_e < 1/(2f)^2$. For a typical f -number $f/8$ this estimate leads to $\delta N/N = e\phi_0/T_e < 4 \cdot 10^{-3}$, i.e. $(2e\phi_0/T_e)^{1/2} < 9 \cdot 10^{-2}$. Therefore, only the lowest amplitude simulation cases considered in this paper may be affected by electron side-loss detrapping (see amplitudes in Figs. 10, 11, and 12).

Concerning ions, one notes that $\tau_{s,l}\omega_{b,i} = (ZT_e/T_i)^{1/2}\tau_{s,l}\omega_{b,e}$. As one always has $ZT_e/T_i > 1$, the characteristic side-loss time in units of the bounce period is in any case larger for ions than for electrons. However, as ion trapping only contributes significantly to the frequency shifts for $ZT_e/T_i \lesssim 15$ (see Fig. 3), side-loss detrapping should in fact similarly affect ions and electrons at these lower temperature ratios. But in all cases, the effect of both electron and ion side-loss detrapping appears to remain a marginal effect for IAWs.

b. Collisional Detrapping in an IAW

In general, three collisional dynamics effects may lead to detrapping: (1) Slowing-down (drag), (2) parallel diffusion, and (3) transverse diffusion (pitch-angle scattering). For collisions of species a on species b , assumed to be at thermal equilibrium and represented by a Maxwellian distribution with density N_b and temperature T_b , these effects are represented by the relations [60]:

$$\frac{d}{dt}\langle \mathbf{v} \rangle = -\nu_s^{ab} \mathbf{v}, \quad (\text{A2})$$

$$\frac{d}{dt}\langle (\mathbf{v}_{\parallel} - \langle v_{\parallel} \rangle)^2 \rangle = \nu_{\parallel}^{ab} v^2, \quad (\text{A3})$$

$$\frac{d}{dt}\langle (\mathbf{v}_{\perp} - \langle v_{\perp} \rangle)^2 \rangle = \nu_{\perp}^{ab} v^2, \quad (\text{A4})$$

where $\langle . \rangle$ stands for a statistical average over a set of particles a , all with the same incoming velocity \mathbf{v} of norm v . The subscripts \parallel and \perp respectively refer to the directions parallel and perpendicular to \mathbf{v} . The collision rates appearing in Eqs. (A2)-(A4) are given by

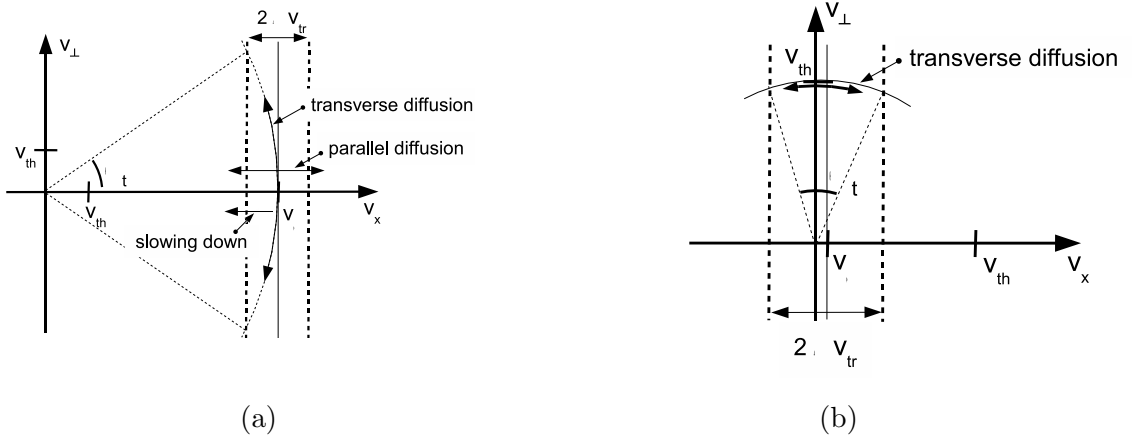


FIG. 20: a) Collisional detrapping in the tail of the distribution. Case of resonant electrons in an EPW or of ions in an IAW. b) Collisional detrapping in the bulk of the distribution. Case of resonant electrons in an IAW.

$$\nu_s^{ab}(v)/\nu_c^{ab}(v) = \left(1 + \frac{m_a}{m_b}\right) \psi(x^{ab}), \quad (\text{A5})$$

$$\nu_{\parallel}^{ab}(v)/\nu_c^{ab}(v) = \frac{\psi(x^{ab})}{x^{ab}}, \quad (\text{A6})$$

$$\nu_{\perp}^{ab}(v)/\nu_c^{ab}(v) = 2 \left[\left(1 - \frac{1}{2x^{ab}}\right) \psi(x^{ab}) + \psi'(x^{ab}) \right], \quad (\text{A7})$$

where $\psi(x) = -(2/\sqrt{\pi})\sqrt{x}\exp(-x) + \text{erf}(\sqrt{x})$ and $\psi'(x) = d\psi/dx = (2/\sqrt{\pi})\sqrt{x}\exp(-x)$ with argument $x^{ab} = m_b v^2 / 2T_b = v^2 / 2v_{\text{th},b}^2$. The basic collision frequency ν_c^{ab} appearing in Eqs. (A5)-(A7) is given by

$$\nu_c^{ab}(v) = \frac{q_a^2 q_b^2 \log \Lambda_{ab} N_b}{4\pi \epsilon_0^2 m_a^2 v^3},$$

where $\log \Lambda_{ab}$ stands for the collision logarithm.

In the case of an IAW, ion trapping occurs for velocities $v_{\phi} - \Delta v_{\text{tr},i} < v_x < v_{\phi} + \Delta v_{\text{tr},i}$ out in the tail of the distribution (see Fig. 2.a). Recall that $v_{\text{th},i}/c_s = (ZT_e/T_i)^{-1/2}$ and $\Delta v_{\text{tr},i}/c_s = 2(e\phi_0/T_e)^{1/2}$, so that in most cases one has the ordering $v_{\phi} \simeq c_s \gg v_{\text{th},i}, \Delta v_{\text{tr},i}$. As shown in Fig. 20.a, collisions may thus lead to ion detrapping by all three effects: drag, as well as parallel and transverse diffusion. For the electron dynamics, one however has the relations $c_s/v_{\text{th},e} = (Zm_e/m_i)^{1/2}$ and $\Delta v_{\text{tr},e}/v_{\text{th},e} = 2(e\phi_0/T_e)^{1/2}$, leading to the typical ordering $v_{\phi} \ll \Delta v_{\text{tr},e} \ll v_{\text{th},e}$. Trapping of electrons thus occurs in the bulk of the

distribution, as shown in Fig. 2.b, and only transverse diffusion may lead to collisional detrapping, as shown in Fig. 20.b.

Considering Fig. 20.b and Eq. (A4), the characteristic time τ_{\perp}^e for electron detrapping by pitch angle scattering may be estimated as $\tau_{\perp}^e \simeq \theta_t^2 / \nu_{\perp}^e(v_{\text{th},e}) \simeq (\Delta v_{\text{tr},e} / v_{\text{th},e})^2 / \nu_{\perp}^e(v_{\text{th},e})$, where the transverse diffusion collision rate includes both contributions from electron-electron as well as electron-ion collisions:

$$\begin{aligned} \nu_{\perp}^e(v_{\text{th},e}) &= \nu_{\perp}^{ee}(v_{\text{th},e}) + \nu_{\perp}^{ei}(v_{\text{th},e}) \\ &\simeq 2\nu_c^{ee}(v_{\text{th},e})\sqrt{\frac{2}{\pi}}\exp(-1/2) + 2\nu_c^{ei}(v_{\text{th},e}) \simeq \nu_c^{ei}(v_{\text{th},e})\left(\frac{1}{Z} + 2\right), \end{aligned}$$

having used the scaling $v_{\text{th},e}/v_{\text{th},i} \gg 1$, relation $\nu_c^{ei}(v_{\text{th},e}) = Z\nu_c^{ee}(v_{\text{th},e})$ and the approximation $2\sqrt{2/\pi}\exp(-1/2) \simeq 1$. The condition for electron detrapping by transverse collisional diffusion to become significant, i.e. $\tau_{\perp}^e \omega_{b,e} < 2\pi$, then leads to the relation

$$\left(\frac{e\phi_0}{T_e}\right)^{3/2} k\lambda_{ei}(v_{\text{th},e}) < 2\pi \frac{1/Z + 2}{4} \simeq 2\pi, \quad (\text{A8})$$

where the thermal electron-ion collision mean free path is defined as $\lambda_{ei}(v_{\text{th},e}) = v_{\text{th},e} / \nu_c^{ei}(v_{\text{th},e})$.

Considering Fig. 20.a, the characteristic time τ_{\perp}^i for ion detrapping by pitch angle scattering is estimated as $\tau_{\perp}^i = \theta_t^2 / \nu_{\perp}^i(c_s) \simeq (2\Delta v_{\text{tr},i} / c_s) / \nu_{\perp}^i(c_s)$, having used $\Delta v_{\text{tr},i} / c_s = 1 - \cos \theta_t \simeq \theta_t^2 / 2$. The transverse diffusion collision rate in general would include both contributions from ion-ion as well as ion-electron collisions, but for ion velocities of order c_s , they scale with the ratio $1 : (1/Z)(Zm_e/m_i)^{1/2}$ and the latter contribution is thus negligible, so that

$$\nu_{\perp}^i(c_s) \simeq \nu_{\perp}^{ii}(c_s) \simeq 2\nu_c^{ii}(c_s).$$

The condition for ion detrapping by transverse collisional diffusion to become significant, i.e. $\tau_{\perp}^i \omega_{b,i} < 2\pi$, then leads to the relation

$$\frac{e\phi_0}{T_e} k\lambda_{ei}(v_{\text{th},e}) < 2\pi, \quad (\text{A9})$$

where the ion-ion collision mean free path evaluated at c_s is defined as $\lambda_{ii}(c_s) = c_s / \nu_c^{ii}(c_s)$ and noting that one in fact has $\lambda_{ii}(c_s) = \lambda_{ei}(v_{\text{th},e})$.

Considering again Fig. 20.a as well as Eq. (A3), the characteristic time τ_{\parallel}^i for ion detrapping by parallel diffusion is estimated as $\tau_{\parallel}^i = (\Delta v_{\text{tr},i} / c_s)^2 / \nu_{\parallel}^i(c_s)$. In general, the

parallel diffusion collision rate would as well include both contributions from ion-ion as well as ion-electron collisions, but for ion velocities of order c_s , they scale with the ratio $T_i/ZT_e : (1/Z)(Zm_e/m_i)^{1/2}$ and the latter contribution is thus again negligible, so that

$$\nu_{\parallel}^i(c_s) \simeq \nu_{\parallel}^{ii}(c_s) \simeq 2\nu_c^{ii}(c_s) \left(\frac{v_{\text{th},i}}{c_s} \right)^2.$$

The condition for ion detrapping by parallel collisional diffusion to become significant, i.e. $\tau_{\parallel}^i \omega_{b,i} < 2\pi$, then leads to the relation

$$\left(\frac{e\phi_0}{T_e} \right)^{3/2} k\lambda_{ei}(v_{\text{th},e}) < 2\pi \frac{1}{2} \frac{T_i}{ZT_e}. \quad (\text{A10})$$

Finally, considering once again Fig. 20.a as well as Eq. (A2), the characteristic time τ_s^i for ion detrapping by collisional drag is estimated as $\tau_s^i = (\Delta v_{\text{tr},i}/c_s)/\nu_s^i(c_s)$. The ion-ion and ion-electron collisional contributions to $\nu_s^i(c_s)$ scale with the ratio $1 : (Zm_e/m_i)^{1/2}$ and the latter contribution can thus once again be neglected, so that

$$\nu_s^i(c_s) \simeq \nu_s^{ii}(c_s) \simeq 2\nu_c^{ii}(c_s).$$

The condition for ion detrapping by collisional drag to become significant, i.e. $\tau_s^i \omega_{b,i} < 2\pi$, then leads to the relation

$$\frac{e\phi_0}{T_e} k\lambda_{ei}(v_{\text{th},e}) < 2\pi, \quad (\text{A11})$$

which is the same constraint as given by Eq. (A9) for collisional ion detrapping by transverse diffusion.

Considering Eqs. (A8)-(A11), it appears that the most significant collisional detrapping effects are electron detrapping by transverse diffusion and ion detrapping by parallel diffusion, both requiring essentially the constraint:

$$\left(\frac{e\phi_0}{T_e} \right)^{3/2} k\lambda_{ei}(v_{\text{th},e}) < 2\pi, \quad (\text{A12})$$

as ion trapping is only effective for lower values of ZT_e/T_i . By evaluating Eq. (A12) in a Helium plasma with $T_e = 2.5$ keV and $N_e = 9 \times 10^{20} \text{ cm}^{-3}$ (typical parameters in a ICF plasma), the limit on $e\phi_0/T_e < 2 \cdot 10^{-2}$, i.e. $(e\phi_0/T_e)^{1/2} < 0.2$, is obtained, a limit only about twice that imposed by sideloss. Note that the ion-ion mean free path has a strong dependence on the charge state and the electron temperature.

Acknowledgments

This work was performed under the auspices of the U.S. Department of Energy by Lawrence Livermore National Laboratory under contract number DE-AC52-07NA27344. This work was partially funded by the Laboratory Directed Research and Development Program at LLNL under project tracking code 08-ERD-031 and 12-ERD-061.

-
- [1] B. I. Cohen, B. F. Lasinski, A. B. Langdon, and E. A. Williams, Phys. Plasmas **4**, 956 (1997).
 - [2] C. Riconda, A. Heron, D. Pesme, S. Huller, V. T. Tikhonchuk, and F. Detering, Phys. Rev. Lett. **94**, 055003 (2005).
 - [3] C. Riconda, A. Heron, D. Pesme, S. Huller, V. T. Tikhonchuk, and F. Detering, Phys. Plasmas **12**, 112308 (2005).
 - [4] D. Pesme, C. Riconda, and V. T. Tikhonchuk, Phys. Plasmas **12**, 092101 (2005).
 - [5] L. Divol, B. I. Cohen, E. A. Williams, A. B. Langdon, and B. F. Lasinski, Phys. Plasmas **10**, 3728 (2003).
 - [6] L. Divol, B. I. Cohen, E. A. Williams, A. B. Langdon, B. F. Lasinski, D. Froula, and S. H. Glenzer, Phys. Plasmas **10**, 1822 (2003).
 - [7] L. Divol, E. A. Williams, B. I. Cohen, A. B. Langdon, and B. F. Lasinski, in *Proceedings of the Third International Conference on Inertial Fusion Sciences and Applications (IFSA2003)* (2003).
 - [8] E. A. Williams, B. I. Cohen, L. Divol, M. R. Dorr, J. A. Hittinger, D. E. Hinkel, A. B. Langdon, R. K. Kirkwood, D. H. Froula, and S. H. Glenzer, Phys. Plasmas **11**, 231 (2004).
 - [9] B. I. Cohen, L. Divol, A. B. Langdon, and E. A. Williams, Phys. Plasmas **12**, 052703 (2005).
 - [10] B. I. Cohen, L. Divol, A. B. Langdon, and E. A. Williams, Phys. Plasmas **13**, 022705 (2006).
 - [11] B. I. Cohen, E. A. Williams, and H. X. Vu, Phys. Plasmas **14**, 102707 (2007).
 - [12] R. R. Lindberg, A. E. Charman, and J. S. Wurtele, Phys. Plasmas **14**, 122103 (2007).
 - [13] R. R. Lindberg, A. E. Charman, and J. S. Wurtele, Phys. Plasmas **15**, 055911 (2008).
 - [14] N. A. Yampolsky and N. J. Fisch, Phys. Plasmas **16**, 072104 (2009).
 - [15] I. Y. Dodin and N. J. Fisch, Phys. Plasmas **19**, 012102 (2012).
 - [16] I. Y. Dodin and N. J. Fisch, Phys. Plasmas **19**, 012103 (2012).
 - [17] I. Y. Dodin and N. J. Fisch, Phys. Plasmas **19**, 012104 (2012).
 - [18] J. Fahlen, B. Winjum, T. Grismayer, and W. Mori, Phys. Rev. Lett. **102**, 245002 (2009).
 - [19] D. Benisti, O. Morice, L. Gremillet, E. Siminos, and D. J. Strozzi, Phys. Plasmas **17**, 030701 (2010).
 - [20] H. Vu, D. DuBois, and B. Bezzerides, Phys. Rev. Lett. **86**, 4306 (2001).
 - [21] H. A. Rose and D. A. Russell, Phys. Plasmas **8**, 4784 (2001).

- [22] S. Brunner and E. J. Valeo, Phys. Rev. Lett. **93**, 145003 (2004).
- [23] H. X. Vu, L. Yin, D. F. DuBois, B. Bezzerides, and E. S. Dodd, Phys. Rev. Lett. **95**, 245003 (2005).
- [24] H. A. Rose, Phys. Plasmas **12**, 012318 (2005).
- [25] M. Albrecht-Marc, A. Ghizzo, T. W. Johnston, T. Reveille, D. D. Sarto, and P. Bertrand, Phys. Plasmas **14**, 072704 (2007).
- [26] D. J. Strozzi, E. A. Williams, A. B. Langdon, and A. Bers, Phys. Plasmas **14**, 013104 (2007).
- [27] L. Yin, B. J. Albright, K. J. B. and W. Daughton, and H. A. Rose, Phys. Rev. Lett. **99**, 265004 (2007).
- [28] D. Benisti and L. Gremillet, Phys. Plasmas **14**, 042304 (2007).
- [29] D. Benisti, D. J. Strozzi, and L. Gremillet, Phys. Plasmas **15**, 030701 (2008).
- [30] J. W. Banks, R. L. Berger, S. Brunner, B. I. Cohen, and J. A. F. Hittinger, Phys. Plasmas **18**, 052102 (2011).
- [31] D. Benisti, O. Morice, L. Gremillet, A. Friou, and E. Lefebvre, Phys. Plasmas **19**, 056301 (2012).
- [32] D. Benisti, N. A. Yampolsky, and N. J. Fisch, Phys. Plasmas **19**, 013110 (2012).
- [33] J. Lindl, P. Amendt, R. L. Berger, S. G. Glendinning, S. H. Glenzer, S. Haan, R. L. Kauffman, O. Landen, and L. J. Suter, Phys. Plasmas **11**, 339 (2004).
- [34] S. H. Glenzer, D. H. Froula, L. Divol, M. Dorr, R. L. Berger, S. Dixit, B. A. Hammel, C. Haynam, J. A. Hittinger, J. P. Holder, O. S. Jones, D. H. Kalantar, O. L. Landen, A. B. Langdon, S. Langer, B. J. MacGowan, A. J. Mackinnon, N. Meezan, E. I. Moses, C. Niemann, C. H. Still, L. J. Suter, R. J. Wallace, E. A. Williams, and B. K. F. Young, Nature Physics (2007).
- [35] D. H. Froula, L. Divol, R. A. London, R. L. Berger, T. Doppner, N. B. Meezan, J. Ralph, J. S. Ross, L. J. Suter, and S. H. Glenzer, Phys. Plasmas **17**, 056302 (2010).
- [36] S. Glenzer, B. MacGowan, P. Michel, N. Meezan, L. Suter, S. Dixit, J. Kline, G. Kyrala, D. Bradley, D. A. Callahan, et al., Science **327**, 1228 (2010).
- [37] H. Schamel, Phys. Plasmas **19**, 020501 (2011).
- [38] B. N. Breizman, Nucl. Fusion **50**, 084014 (2010).
- [39] P. F. Schmit, I. Y. Dodin, and N. J. Fisch, Phys. Plasmas **18**, 042103 (2011).
- [40] I. B. Bernstein, J. M. Greene, and M. D. Kruskal, Phys. Review **108**, 546 (1957).

- [41] T. M. O’Neil, Phys. Fluids **8**, 2255 (1965).
- [42] G. J. Morales and T. O’Neil, Phy. Rev. Lett. **28**, 417 (1972).
- [43] R. L. Dewar, Phys. Fluids **15**, 712 (1972).
- [44] B. Winjum, J. Fahlen, and W. Mori, Phys. Plasmas **14**, 102104 (2007).
- [45] K. Estabrook, W. L. Kruer, and M. G. Haines, Phys. Fluids B **1**, 1282 (1989).
- [46] D. C. Barnes, Phys. Plasmas **11**, 903 (2004).
- [47] W. Manheimer and R. W. Flynn, Phys. Fluids **14**, 2393 (1971).
- [48] R. L. Berger, C. H. Still, E. A. Williams, and A. B. Langdon, Phys. Plasmas **5**, 4337 (1998).
- [49] C. H. Still, R. L. Berger, A. B. Langdon, D. E. Hinkel, L. J. Suter, and E. A. Williams, Phys. Plasmas **7**, 2023 (2000).
- [50] D. E. Hinkel, M. D. Rosen, E. A. Williams, A. B. Langdon, C. H. Still, D. A. Callahan, J. D. Moody, P. A. Michel, R. P. J. Town, R. A. London, and S. H. Langer, Phys. Plasmas **18**, 056312 (2011).
- [51] R. L. Dewar, W. L. Kruer, and W. M. Manheimer, Phy. Rev. Lett. **28**, 215 (1972).
- [52] S. Brunner, E. Valeo, B. Still, R. Berger, D. Strozzi, E. Williams, and J. Hittinger, Tech. Rep., LLNL (2008).
- [53] C. Z. Cheng and G. Knorr, J. Comp. Phys. **22**, 330 (1976).
- [54] A. Ghizzo, B. Izrar, P. Bertrand, E. Fijalkow, M. R. Feix, and M. Shoucri, Phys. Fluids **31**, 72 (1988).
- [55] M. M. Shoucri and R. R. J. Gagné, J. Comp. Phys. **27**, 315 (1978).
- [56] A. Ghizzo, P. Bertrand, M. M. Shoucri, T. W. Johnston, E. Fijalkow, and M. R. Feix, J. Comp. Phys. **90**, 431 (1990).
- [57] P. Bertrand, A. Ghizzo, T. W. Johnson, M. Shoucri, E. Fijalkow, and M. R. Feix, Phys. Fluids B **2**, 1028 (1990).
- [58] D. J. Strozzi, M. M. Shoucri, and A. Bers, Computer Physics Communications **164**, 156 (2004), ISSN 0010-4655, proceedings of the 18th International Conferene on the Numerical Simulation of Plasmas.
- [59] A. Vlasov, J. Phys. (USSR) **9**, 25 (1945).
- [60] B. A. Trubnikov, *Particle Interactions in a Fully Ionized Plasma* (M. A. Leontovich, Consultants Bureau, New York, 1965), vol. 1 of *Reviews of Plasma Physics*, p. 105.